

THEORETICAL TRANSMISSION SPECTRA OF EXOPLANET ATMOSPHERES WITH HYDROCARBON HAZE: EFFECT OF CREATION, GROWTH, AND SETTLING OF HAZE PARTICLES. I. MODEL DESCRIPTION AND FIRST RESULTS

YUI KAWASHIMA^{1, 2} AND MASAHIRO IKOMA^{1, 3}

¹Department of Earth and Planetary Science, Graduate School of Science, The University of Tokyo, 7-3-1 Hongo, Bunkyo-ku, Tokyo 113-0033, Japan

²ykawashima@eps.s.u-tokyo.ac.jp

³Research Center for the Early Universe (RESCEU), Graduate School of Science, The University of Tokyo, 7-3-1 Hongo, Bunkyo-ku, Tokyo 113-0033, Japan

ABSTRACT

Recently, properties of exoplanet atmospheres have been constrained via multi-wavelength transit observation, which measures an apparent decrease in stellar brightness during planetary transit in front of its host star (called transit depth). Sets of transit depths so far measured at different wavelengths (called transmission spectra) are somewhat diverse: Some show steep spectral slope features in the visible, some contain featureless spectra in the near-infrared, some show distinct features from radiative absorption by gaseous species. These facts infer the existence of haze in the atmospheres especially of warm, relatively low-density super-Earths and mini-Neptunes. Previous studies that addressed theoretical modeling of transmission spectra of hydrogen-dominated atmospheres with haze used some assumed distribution and size of haze particles. In this study, we model the atmospheric chemistry, derive the spatial and size distributions of haze particles by simulating the creation, growth and settling of hydrocarbon haze particles directly, and develop transmission spectrum models of UV-irradiated, solar-abundance atmospheres of close-in warm (~ 500 K) exoplanets. We find that the haze is distributed in the atmosphere much more broadly than previously assumed and consists of particles of various sizes. We also demonstrate that the observed diversity of transmission spectra can be explained by the difference in the production rate of haze monomers, which is related to the UV irradiation intensity from host stars.

Keywords: planets and satellites: atmospheres — planets and satellites: composition — planets and satellites: individual (GJ 1214b)

1. INTRODUCTION

Composition of exoplanet atmospheres is often measured by transit observation (e.g., Seager & Deming 2010). When transiting in front of its host star, a planet blocks a fraction of the incident stellar light. The amount of blocked light relative to the original stellar light is called the transit depth. Since a set of transit depths observed at different wavelengths (called transmission spectrum) depends on atmospheric constituents, one can infer the atmospheric composition via multi-wavelength transit observations.

Recently, thanks to advance in observational techniques, atmospheric characterization for relatively small planets has become possible via transit observations. Typical examples are GJ 1214b of mass $6.26 M_{\oplus}$ and radius $2.80 R_{\oplus}$ (Charbonneau et al. 2009; Anglada-Escudé et al. 2013), GJ 3470b of $13.73 M_{\oplus}$ and

$3.88 R_{\oplus}$ (Biddle et al. 2014), and GJ 436b of $25.4 M_{\oplus}$ and $4.10 R_{\oplus}$ (Lanotte et al. 2014). Interestingly, transmission spectra of those planets observed so far cannot be explained only by absorption and scattering (i.e., extinction) of gaseous molecules in the atmospheres.

GJ 1214b is a super-Earth whose atmosphere has been probed most. Recent multi-wavelength transit observations show a relatively featureless or flat spectrum from the optical (e.g. Narita et al. 2013; Nascimbeni et al. 2015) to near-infrared (e.g. Kreidberg et al. 2014), although de Mooij et al. (2012) reported a tentative increase in the transit depth in the optical. This raises the possibility that particles such as clouds and hazes are present in the atmosphere, because those particles obscure molecular absorption features. (In this study, we refer to thermochemical condensates as “clouds” and photochemical products as “hazes”.) Also, its transmission spectrum in the near-infrared is too flat to

be explained even by a CO₂-dominated atmosphere (Kreidberg et al. 2014). GJ 436b is also reported as showing a featureless spectrum in the near-infrared by Knutson et al. (2014), suggesting the presence of a cloudy/hazy layer.

GJ 3470b is reported to show a bit more complicated spectrum, which includes a steep spectral slope¹ in the optical (Fukui et al. 2013; Nascimbeni et al. 2013; Biddle et al. 2014; Dragomir et al. 2015; Awiphan et al. 2016) and is relatively featureless or flat in the near-infrared (Crossfield et al. 2013; Ehrenreich et al. 2014). A modest amount of cloud/haze particles, if present, tend to steepen the spectral slope in the optical (Lecavelier Des Etangs et al. 2008), while a thick cloud/haze obscures molecular and atomic absorption features, flattening the spectrum. Though the number of samples is still small, cloud/haze may be commonly present and bring about a diversity of spectra (Sing et al. 2016). Stevenson (2016) and Heng (2016) explored this diversity by quantifying the degree of cloudiness in atmospheres of transiting exoplanets from their spectra. Both two studies reported the trend that cooler planets were more likely to have cloudy/hazy atmospheres.

As a candidate for the cloud/haze, we consider hydrocarbon haze in this study for the reason below, while some other constituents are assumed in previous studies. The above three exoplanets are close-in super-Earths/mini-Neptunes orbiting M stars. Their atmospheric temperatures are typically ~ 500 to 1000 K. Also, those close-in planets are exposed to intense UV radiation from their host stars. In such warm, highly-UV irradiated environments, hydrocarbon hazes are formed easily through photochemical reactions triggered by photo-dissociation of methane, provided the atmospheres are reducing enough that CH₄ rather than CO dominates the atmospheric carbon chemistry (e.g. Yung et al. 1984). Note that a great number of exoplanets in the similar environments will be detected in near future, because MK dwarfs are most abundant in the solar neighborhood (e.g., Cantrell et al. 2013). Also, transit exoplanet surveys so far have detected many low-density low-mass exoplanets, which indicates that there are abundant low-mass exoplanets with relatively hydrogen-rich, reducing atmospheres (Fortney et al. 2007, and references therein).

Some studies so far addressed theoretical modeling of transmission spectra of hydrogen-rich atmospheres

in such environments, considering the effect of haze in the atmosphere. Howe & Burrows (2012) is the first to quantify the effects of haze on transmission spectrum of GJ 1214b’s atmosphere. They assumed an atmospheric layer that contained haze particles such as tholin. The haze layer is characterized by four parameters, including single values of the number density and size of the haze particles and the pressures of the upper and lower edges of the haze layer. (They also considered the existence of clouds, below which transmitted light is cut off completely, regardless of wavelength.) Comparing their theoretical spectra with various haze/cloud properties and molecular compositions to the observed transmission spectrum of GJ 1214b, they demonstrated that a hydrogen-rich atmosphere with the haze layer could explain the observed transmission spectrum, provided appropriate sets of the haze parameters were chosen.

The same way for incorporating the effect of a haze layer was adopted by Ehrenreich et al. (2014), who modeled transmission spectra of GJ 3470b’s atmosphere and then compared them with the observed one, including their observations done with *Hubble* Space Telescope (HST). They found no solution that reproduced the observed steep spectral slope in the optical, simultaneously with the observed flat spectrum in the near-infrared. Instead, they concluded that both of the observed features in the visible and the near-infrared could be matched by a hydrogen-rich atmosphere covered with clouds, which they modeled in the same way as Howe & Burrows (2012).

In contrast to the above theoretical modelings that *assume* the altitude and thickness of the haze layer, Morley et al. (2013) tried to determine those properties by doing photochemical calculations. They derived numerically the vertical distributions of the photochemically-produced hydrocarbons, HCN, C₂H₂, C₂H₄, and C₂H₆, which are precursors of haze particles. Assuming that haze particles formed from a given fraction of the precursors, which they regarded as a parameter (called the haze-forming efficiency), they determined the distribution of haze particles and then modeled the transmission spectrum of GJ 1214b’s atmosphere with assumed particle size and number density. (In their modeling, they used the opacity data of soot instead of those of tholin.) They found that the observed transmission spectra of GJ 1214b could be explained by the haze particles with the size of 0.01 to $0.25 \mu\text{m}$ and the haze-forming efficiency of $1\text{-}5\%$, although there remained a possibility of clouds composed of KCl and ZnS.

The above studies certainly demonstrated that theoretical transmission spectra of hazy atmospheres matched the corresponding observations for appropriate choices of the haze parameters. However, they did not access the viability of those haze properties sufficiently

¹ The steep slope in the optical is sometimes referred to as the Rayleigh scattering slope in the literature. However, one can never conclude that the slope is due to Rayleigh scattering from an observed spectral slope alone (see Heng 2016).

from a physical point of view. In addition, transmission spectra so far observed seem to be diverse (Sing et al. 2016): In the visible, some show distinct spectral slope features, some may not. Also, some show molecular and atomic features, some are featureless. Again, although the previous studies found that choice of various haze parameters resulted in variation in transmission spectra, it remains to be clarified what yields such a variety of haze properties.

Of special interest in this study is the distribution of the size and number density of haze particles and its impacts on transmission spectra, which have not been investigated previously. Therefore we develop transmission spectrum models with detailed calculations of the creation, growth, and settling of hydrocarbon haze particles, assuming hydrogen-dominated atmospheres of close-in warm ($\lesssim 1000$ K) exoplanets. In this first paper, we focus on describing the methodology and demonstrating the sensitivity of transmission spectra to the production rate of haze monomers, which relates to the amount of UV irradiation from the host star. In our forthcoming papers, we make detailed investigation of the dependence of transmission spectra on model parameters, other than monomer production rate, such as atmospheric metallicity, C/O ratio, eddy diffusion coefficient, atmospheric temperature profile, and monomer size. Also, we explore in detail the composition of the atmospheres of known warm exoplanets by comparing the observed spectra with our theoretical ones, taking into account other possibilities of cloud/haze constituents.

The rest of this paper is organized as follows. In § 2, we describe the assumptions, equations, and calculation methods for the size and number density distributions of haze particles and generating the transmission spectra. In § 3, we investigate the vertical distribution of haze particles and its effects on the transmission spectra. Also, we investigate the dependence of the spectra on the production rate of haze monomers, which is related to UV irradiation intensity from the host star. In § 4, to gain a deeper understanding of the effect of the haze particle distribution on transmission spectrum, we calculate the particle growth and transmission spectra with a characteristic-size approximation and then compare the results with those obtained in § 3. Finally, we conclude this paper in § 5.

2. MODEL AND METHOD DESCRIPTION

As described in Introduction, we develop transmission spectrum models of warm transiting planets with hydrogen-rich atmospheres by incorporating the effects of the size and number density distributions of hydrocarbon haze that are determined through the production, growth, and settling processes of the particles. First, precursor molecules of haze particles (i.e., higher-order

hydrocarbons, which we call haze precursors, hereafter) are created through photochemical reactions triggered by UV photodissociation of CH_4 . Then, aggregation of the haze precursors results in haze particles of small size, which are called monomers. Note that the size of monomers in the atmosphere of Titan was reported as 40 ± 10 nm from observations (Tomasko et al. 2009). Those monomers diffuse and settle downward. Also, collisional growth of the haze particles takes place. Once the haze particles go down into hot, convective regions, they are likely to be thermodynamically broken and evaporated to be CH_4 again, which can be diffused upward to be the source of haze precursors.

In this study, we first perform photochemical calculations to derive the vertical distribution of haze precursors in a similar way to Morley et al. (2013) (§ 2.1). Then, using the obtained vertical profiles of the precursors, we calculate the growth and settling of haze particles in the atmosphere to derive the steady-state distributions of the size and number density of the haze particles (§ 2.2). Finally, we calculate the extinction opacities of the gases and particles (§ 2.3) and model transmission spectra of the atmospheres with obtained properties of haze (§ 2.4).

Before explaining the details of the above three modules, we first describe the assumptions and treatments made in all the modules. We make a reasonable assumption that the atmosphere is in hydrostatic equilibrium and composed of ideal gases. While considering the altitude variation of gravity for hydrostatic structure, we neglect the effect of curvature, which would yield only a small difference compared to other large uncertainties in model parameters, and assume plane-parallel structure in the photochemical and particle growth calculations. In this paper, because our focus is on the effects of the size distribution of haze particles on transmission spectra, we assume, for simplicity, that the atmospheric structure is spherically symmetric. In reality, since close-in exoplanets tend to be tidally locked, the structure may be far from spherically symmetric. The details of this effect will be explored in our forthcoming papers.

2.1. Photochemical Model

Various photochemical models have been constructed for terrestrial and gaseous planets. Allen et al. (1981)'s model is for studying the vertical transport and photochemistry in the Earth's mesosphere and lower thermosphere (50-120 km). Using their model, they derived the distributions of long-lived species and compared them with observations. Line et al. (2011) introduced their photochemical model to explore the chemistry of warm gaseous exoplanetary atmospheres for explaining the observed depletion of methane in the atmosphere

of GJ 436b. Venot et al. (2012) released a large chemical network applying combustion models, which were validated over the temperature and pressure ranges relevant to hot Jupiter atmospheres. After that, they expanded their networks to hydrocarbons up to six-order (Venot et al. 2015). Hu et al. (2012) presented the photochemical model for terrestrial exoplanets applicable for all types of atmospheres, from reducing to oxidizing. They presented the results for three benchmark cases of atmospheric scenarios from reducing to oxidizing for terrestrial exoplanets. Tsai et al. (2017) presented an open-source photochemical model for hot exoplanetary atmospheres, VULCAN, which they validated by reproducing the results of Moses et al. (2011). In this study, we newly develop a photochemical model to derive the vertical distribution of haze precursors.

2.1.1. Model description

The one-dimensional continuity-transport equation that governs the change in the number density of species i , n_i , is written as (Yung & Demore 1999)

$$\frac{\partial n_i}{\partial t} = P_i - L_i - \frac{\partial \Phi_i}{\partial z}, \quad (1)$$

where t and z are the time and the altitude, respectively, P_i and L_i are the production and loss rates of species i due to photochemical and thermochemical reactions, respectively, and Φ_i is the vertical transport flux of species i . We assume that the vertical transport occurs by eddy diffusion and ignore molecular diffusion. The eddy diffusion flux is given by (Yung & Demore 1999)

$$\Phi_i = -K_{zz} N \frac{\partial f_i}{\partial z}, \quad (2)$$

where K_{zz} is the eddy diffusion coefficient, N is the total number density of the atmospheric gas molecules, and $f_i \equiv n_i/N$ is the mixing ratio of species i . Here, we have used the definition of atmospheric scale height and the ideal gas law.

We include the following 29 chemical species composed of the five elements, C, H, O, N, and He: O, O₂, H₂O, H, OH, CO₂, CO, HCO, CH₄, CH₃, CH₃O, CH₃OH, CH, CH₂, C, C₂, C₂H, C₂H₂, N, N₂, NH, NH₂, NH₃, CN, HCN, H₂, He, O(¹D), and ¹CH₂. These species are the ones considered in the photochemical models of Kopparapu et al. (2012), who studied the atmosphere of the hot Jupiter WASP-12b, except for H₂CO and CH₂OH, which we do not consider. Since the main focus of this study is on calculating the size and spatial distributions of haze particles and evaluating their impacts on resultant transmission spectra, we simply assume that the haze precursors form from C₂H₂ and HCN, in the same way as Morley et al. (2013), and do not include higher-order hydrocarbons such as C₂H₄ and C₂H₆. They showed that HCN and C₂H₂ are the

most dominant hydrocarbons photochemically produced in solar-abundance atmospheres with temperature of 500-1000 K, although there remains uncertainties for the treatment of higher-order hydrocarbons (see, e.g., Zahnle et al. 2016). Also, we do not consider sulphur compounds, because they are scarcely involved in reactions with hydrocarbons of interest here. As both the opacities of H₂S and OCS are much smaller compared to those of H₂O and CH₄ according to sulphur's small elemental abundance, it is sure that they have little impact on the transmission spectrum. We do not consider Na and K because they condense as Na₂S and KCl clouds, respectively, and settle downward in the temperature range of interest ($\lesssim 1000$ K) (Morley et al. 2013).

We adopt 154 thermochemical reactions from the reaction list of Hu et al. (2012). All the thermochemical reactions and their rate coefficients are listed in Table C1. We have chosen the reactions that involve only some of the above 31 species, although the reaction list of Hu et al. (2012) contains more reactions. We also consider their reverse reactions using the method described in Visscher & Moses (2011). Thus, in total, we consider 308 thermochemical reactions. For the calculation of the Gibbs free energy of each species, which is needed to calculate the equilibrium constants (the ratios of forward to reverse reaction rate coefficients), we use the polynomial coefficients for calculating enthalpies of formation, entropies, and heat capacities from the Third Millennium Ideal Gas and Condensed Phase Thermochemical Database for Combustion². Although some rate coefficients are invalid in the temperature range considered in this study, we use them outside their temperature range due to the lack of data and/or theory.

For photochemistry, we consider 16 reactions listed in Table D2. Likewise, all the reactions are extracted from the reaction list of Hu et al. (2012) if the reaction involves only some of the above 31 species. Photodissociation rate of species i (i.e., the number of atoms or molecules dissociated per unit time) at altitude z , $J_i(z)$, is written as

$$J_i(z) = \frac{1}{2} \int_0^\infty q_i(\lambda) \sigma_i(\lambda) F(z, \lambda) d\lambda, \quad (3)$$

where λ is the wavelength, $q_i(\lambda)$ and $\sigma_i(\lambda)$ are the dimensionless quantum yield of species i , the absorption cross section (its physical dimension being area) of species i , and $F(z, \lambda)$ is the actinic photon flux per unit area, unit time, and unit wavelength. The factor 1/2 is needed to account for diurnal variation (see Hu et al. 2012). The references from which we take the data of the quantum yields and absorption cross sections are tabu-

² <http://garfield.chem.elte.hu/Burcat/burcat.html>

lated in Table E3 and D2, respectively, most of which can be downloaded from the website of the MPI-Mainz UV/VIS Spectral Atlas of Gaseous Molecules of Atmospheric Interest³. Temperature dependences of absorption cross sections are known for some of the species, but measured only in a temperature range between 200 and 300 K. Thus, following Hu et al. (2012), we calculate the absorption cross sections at 300 K by a linear interpolation with the use of the measured data and use them for temperatures higher than 300 K, namely $\sigma(\lambda, T) = \sigma(\lambda, 300 \text{ K})$, instead of extrapolating beyond 300 K. We consider the attenuation of the actinic flux as

$$F(z, \lambda) = F(\infty, \lambda) e^{-\tau(z, \lambda)/\mu}, \quad (4)$$

where $F(\infty, \lambda)$ is the actinic flux at the top of the atmosphere at wavelength λ and μ is the cosine of the zenith angle of the star. $\tau(z, \lambda)$ is the optical depth defined by

$$\tau(z, \lambda) = \sum_i^{\mathcal{N}} \int_z^{\infty} n_i(z') \sigma_i(\lambda) dz', \quad (5)$$

where \mathcal{N} is the number of the species. We assume the zenith angle to be 57.3° , as done in Hu et al. (2012). They found that the mean zenith angle differed depending on the optical depth of interest and concluded that the assumption of $\mu = 57^\circ$ - 48° , which corresponded to $\tau = 0.1$ - 1.0 , was appropriate for the one-dimensional photochemical models.

For the boundary conditions, we set the diffusion flux Φ_i as zero for all the species at the upper boundary, while we fix the volume mixing ratios f_i of all the species at the thermochemical equilibrium values at the lower boundary. The exact conditions are, however, uncertain, so that previous studies chose different conditions at both boundaries. As for the upper boundary condition, while some studies set the diffusion flux equal to the assumed atmospheric escape flux (e.g., Hu et al. 2012), some studies set $\Phi_i = 0$ for all the species (e.g. Moses et al. 2011; Venot et al. 2012; Tsai et al. 2017). In this study, we choose the latter because the atmospheric escape rate is unknown for exoplanets. As for the lower boundary condition, photochemical modeling of terrestrial planet atmospheres often sets the flux of surface emission and/or deposition at the lower boundary (e.g., Hu et al. 2012). However, gas-rich planets, which we consider in this study, have no rigid surfaces. While some studies adopted zero flux (e.g., Moses et al. 2011; Venot et al. 2012; Tsai et al. 2017), we fix the volume mixing ratios f_i of all the species at thermochemical equilibrium values in a similar way to, for example, Line et al. (2011) and Zahnle & Marley (2014). This

is because the gases at deep levels would be in thermochemical equilibrium. While Moses et al. (2011) reported that they did not find any differences in the results between the two types of inner boundary condition, Tsai et al. (2017) found that only the minor ($f_i \lesssim 10^{-9}$) molecules, CO and CO₂, deviated from their thermochemical equilibrium values at relatively cool (1000 K) lower boundary (1000 bar), but major molecules are in thermochemical equilibrium.

2.1.2. Calculation method

The calculation method we use in this study is basically the same as that used in previous works (e.g., Venot et al. 2012; Hu et al. 2012; Tsai et al. 2017). We discretize Eq. (1) as

$$\frac{\partial n_{i,j}}{\partial t} = P_{i,j} - L_{i,j} - \frac{\Phi_{i,j+1/2} - \Phi_{i,j-1/2}}{\Delta z_j}, \quad (6)$$

where the subscript j represents the physical quantities in the j th layer and Δz_j is the thickness of the j th layer. We prepare layers with the same thickness Δz and set the pressure at the mid-point altitude of the lowest layer as the lower boundary pressure. From Eq. (2), we approximate $\Phi_{i,j+1/2}$ as (e.g., Venot et al. 2012; Hu et al. 2012; Tsai et al. 2017)

$$\Phi_{i,j+1/2} = -K_{zz} N_{j+1/2} \frac{f_{i,j+1} - f_{i,j}}{\Delta z}. \quad (7)$$

To obtain a steady-state solution, we solve Eq. (6) implicitly with the use of the solver DLSODES (Hindmarsh 1982), which is suitable to solve stiff ODE systems such as chemical network calculations (e.g., Grassi et al. 2014). It is based on a backward differentiation formula (BDF), which is also called Gear's method. The most suitable order is chosen within the solver. We set the maximum order allowed to be five. We adopt the values of relative (RTOL) and absolute (ATOL) tolerances as 10^{-4} and $N_j \times 10^{-15}$, respectively; the value of ATOL differs from layer to layer.

The initial number densities of the species are set to their thermochemical equilibrium values, which we calculate in the following way. A system composed of \mathcal{N} gaseous species being considered, the Gibbs free energy of the system is minimized at equilibrium. The Gibbs free energy at fixed temperature T , pressure P , and composition ξ is written as (Smith & Missen 1982)

$$G(T, P, \xi) = \sum_{i=1}^{\mathcal{N}} \xi_i \phi_i, \quad (8)$$

where ξ_i and ϕ_i are the molar number and chemical potential of species i , respectively, and $\xi = \{\xi_1, \xi_2, \dots, \xi_{\mathcal{N}}\}$. The chemical potential of an ideal gas is given by (Smith & Missen 1982)

$$\phi_i(T, P) = \phi_i^\circ(T) + \mathcal{R}T \ln \frac{P_i}{P_{\text{ref}}}. \quad (9)$$

³ <http://satellite.mpic.de/spectralAtlas>

Here ϕ° is the standard chemical potential that is a function of T only, p_i is the partial pressure of gaseous species i , p_{ref} is the reference pressure, and \mathcal{R} is the molar gas constant. If a collection of species in the system is given, theoretically permissible chemical reactions can be derived from the law of conservation of mass:

$$\sum_{i=1}^{\mathcal{N}} a_{ki} \xi_i = b_k, \quad (10)$$

where a_{ki} is the number of the k th element contained in species i and b_k is the total number of moles of the k th element. The composition that gives the minimum value of the Gibbs free energy is searched for to determine the equilibrium values of the mole fractions of the elements in the system. We assume vertically constant elemental abundance ratios and use the same Gibbs free energy data as that we use for calculation of reverse rate coefficients.

We time-integrate Eq. (6) until the system becomes in a steady state. We adopt the criteria of convergence such that all the species of $f_i > 10^{-10}$ vary in mixing ratio by less than 1% in all the layers. The integration is done over a period longer than the eddy diffusion timescale, which we assume as the maximum value of H_j^2/K_{zz} among all the layers at the initial condition. Here, H_j is the atmospheric scale height for layer j . The time step is self-adjusted within the solver so that the estimated local error in $n_{i,j}$ is not larger by an order of magnitude than that of $\text{RTOL} \times n_{i,j} + \text{ATOL}_j$ ($\equiv \text{EWT}_{i,j}$). At each time after calling the solver, for the atmosphere to be in hydrostatic equilibrium and the total mixing ratio to be unity, we set the output negative number densities to be zero, renormalize the volume mixing ratio of each species, recalculate the total number density at each layer assuming hydrostatic equilibrium, and calculate the number density of each species at each layer. Note that the output negative number densities are not larger by an order of magnitude than EWT.

We compare our photochemical model with the previous thermochemical models for the atmospheres of HD 189733b and HD 209458b presented by Tsai et al. (2017) in APPENDIX A and the photochemical models for the WASP-12b's atmosphere presented by Kopparapu et al. (2012) in APPENDIX B. We have confirmed that the abundances of most of the species match those of the previous works within one order of magnitude and the profiles of the molecules are similar except for absolute value. And the differences in abundances for some molecules would not affect our results regarding haze distributions and transmission spectra. We have also confirmed the major trend found in those for GJ 1214b's atmosphere (Miller-Ricci Kempton et al.

2012; Morley et al. 2013) and other low temperature ($\lesssim 1000$ K) atmospheres (Moses et al. 2013; Venot et al. 2014).

2.2. Particle Growth Model

We simulate the growth and settling of hydrocarbon haze particles after the production of monomers in the upper atmosphere and determine their steady-state distribution. We assume that monomers form in situ from the precursor molecules of haze particles. We assume HCN and C_2H_2 as the precursor molecules. While higher-order hydrocarbons may have to be also included as the precursors, previous studies (e.g., Morley et al. 2013) showed that HCN and C_2H_2 are the most dominant hydrocarbons photochemically produced in solar abundance atmospheres with temperature of 500-1000 K, as mentioned in § 2.1.

2.2.1. Model description

We follow the classical formalism for cloud particle growth (see Jacobson 2005), which has also been used to simulate haze particle growth in Titan's atmosphere (e.g., Toon et al. 1980, 1992). Note that the same formalism has been also used for dust particle growth in the field of planet formation (see, e.g., Armitage 2010). Also, as for dust particle growth for brown dwarf atmospheres, there is a series of work (Woitke & Helling 2003, 2004; Helling & Woitke 2006), which is different from ours in the point that they considered particle growth due to chemical surface reactions but did not consider the growth due to coagulation.

Adopting a discrete volume grid, one can write the one-dimensional continuity-transport equation for the number density of particles with volume v_i , $n(v_i)$, as (e.g. Lavvas et al. 2010)

$$\begin{aligned} \frac{\partial n(v_i)}{\partial t} = & \frac{1}{2} \sum_{k=1}^{i-1} K(v_k, v_i - v_k) n(v_k) n(v_i - v_k) \\ & - n(v_i) \sum_{k=1}^{\mathcal{N}} K(v_i, v_k) n(v_k) \\ & - \frac{\partial \Phi(v_i)}{\partial z} + p(v_i), \end{aligned} \quad (11)$$

where the subscript denotes the volume grid, $K(v_i, v_k)$ is the coagulation kernel between two particles with volumes v_i and v_k , and \mathcal{N} is the total number of volume bins used in the calculation. The first and second terms on the right-hand side describe the production and loss of the particles of volume v_i (hereafter, the i th particles, for simplicity) due to the coagulation. $\Phi(v_i)$ is the vertical transport flux and $p(v_i)$ is the photochemical production rate of the i th particles, which takes a non-zero value only for v_1 , namely monomers.

Assuming that the vertical transport occurs by sedimentation and eddy diffusion, one can write $\Phi(v_i)$ as (e.g. [Lavvas et al. 2010](#))

$$\Phi(v_i) = -V_{s,i}n(v_i) - K_{zz}N\frac{\partial(n(v_i)/N)}{\partial z}, \quad (12)$$

where $V_{s,i}$ is the sedimentation velocity of the i th particles written as (e.g. [Lavvas et al. 2010](#))

$$V_{s,i} = \frac{2s_i^2\rho_p g}{9\eta_a} f_{\text{slip},i}. \quad (13)$$

Here, s_i is the radius of the i th particle, ρ_p is the particle internal density, and g is the local gravitational acceleration. η_a is the dynamic viscosity defined as

$$\eta_a = \frac{1}{3}\rho_a\bar{V}_{\text{th}}\lambda_a, \quad (14)$$

where ρ_a is the mass density of the gas, \bar{V}_{th} is the thermal velocity of the gaseous molecules defined as

$$\bar{V}_{\text{th}} = \sqrt{\frac{8k_{\text{B}}T}{\pi m_a}} \quad (15)$$

with the Boltzmann constant k_{B} , and the temperature T , and the mean mass of gaseous molecules m_a . λ_a is the atmospheric mean free path defined as

$$\lambda_a = \frac{k_{\text{B}}T}{\pi\sqrt{2}Pd^2} \quad (16)$$

with the pressure P and the diameter of the gas molecule d . Because H_2 is the most abundant gas species in the atmosphere of interest in this study, we use the diameter of H_2 for the value of d , taken from CRC Handbook of CHEMISTRY and PHYSICS ([Haynes 2012](#)). f_{slip} is the Cunningham slip-flow correction factor given by ([Davies 1945](#))

$$f_{\text{slip},i} = 1 + 1.257K_{n,i} + 0.400K_{n,i}\exp(-1.10/K_{n,i}), \quad (17)$$

where $K_{n,i}$ is the Knudsen number defined as $K_{n,i} \equiv \lambda_a/s_i$.

As for coagulation, we consider two rate-controlling processes which include the Brownian diffusion and gravitational collection. The latter is the collisional process that occurs as a result of difference in sedimentation velocity between different size particles. The total kernel is assumed to be the sum of the two kernels, namely

$$K(v_i, v_k) = K_{\text{BD}}(v_i, v_k) + K_{\text{GC}}(v_i, v_k). \quad (18)$$

The Brownian collision kernel for the i th and k th particles, $K_{\text{BD}}(v_i, v_k)$, can be written as ([Jacobson 2005](#))

$$K_{\text{BD}}(v_i, v_k) = \frac{4\pi(s_i + s_k)(D_{p,i} + D_{p,k})}{\frac{s_i + s_k}{s_i + s_k + \sqrt{\delta_i^2 + \delta_k^2}} + \frac{4(D_{p,i} + D_{p,k})}{\sqrt{v_{\text{th},i}^2 + v_{\text{th},k}^2}(s_i + s_k)}} \quad (19)$$

with

$$\delta_i = \frac{(2s_i + \lambda_{p,i})^3 - (4s_i^2 + \lambda_{p,i}^2)^{3/2}}{6s_i\lambda_{p,i}}. \quad (20)$$

$D_{p,i}$ and $\bar{v}_{\text{th},i}$ are the diffusion coefficient and thermal velocity for the i th particle, respectively. These parameters are given as

$$D_{p,i} = \frac{k_{\text{B}}T}{6\pi s_i\eta_a} f_{\text{slip},i} \quad (21)$$

and

$$\bar{v}_{\text{th},i} = \sqrt{\frac{8k_{\text{B}}T}{\pi m_{p,i}}} \quad (22)$$

with the particle mass $m_{p,i}$. $\lambda_{p,i}$ is the particle's mean free path written as

$$\lambda_{p,i} = \frac{8D_{p,i}}{\pi\bar{v}_{\text{th},i}}. \quad (23)$$

The gravitational collection kernel for the i th and k th particles, $K_{\text{GC}}(v_i, v_k)$, can be written as ([Jacobson 2005](#))

$$K_{\text{GC}}(v_i, v_k) = E_{\text{coll},i,k}\pi(s_i + s_k)^2|V_{s,i} - V_{s,k}|, \quad (24)$$

where $E_{\text{coll},i,k}$ is a collision efficiency given by

$$E_{\text{coll},i,k} = \frac{60E_{\text{V},i,k} + E_{\text{A},i,k}\text{Re}_i}{60 + \text{Re}_i} \quad (s_i \geq s_k) \quad (25)$$

$$E_{\text{V},i,k} = \begin{cases} \left[1 + \frac{0.75 \ln(2\text{St}_{i,k})}{\text{St}_{i,k} - 1.214}\right]^{-2} & (\text{St}_{i,k} > 1.214) \\ 0 & (\text{St}_{i,k} \leq 1.214) \end{cases} \quad (26)$$

$$E_{\text{A},i,k} = \frac{\text{St}_{i,k}^2}{(\text{St}_{i,k} + 0.5)^2}. \quad (27)$$

Here, Re_i is the Reynolds number written as

$$\text{Re}_i = \frac{2s_i V_{s,i}}{\nu_a} \quad (28)$$

with the kinematic viscosity

$$\nu_a = \frac{\eta_a}{\rho_a} \quad (29)$$

and $\text{St}_{i,k}$ is the Stokes number written as

$$\text{St}_{i,k} = \frac{V_{s,k}|V_{s,i} - V_{s,k}|}{s_i g} \quad (s_i > s_k). \quad (30)$$

When we simulate the particle growth with the discretized size distribution, we face the problem that the coagulation between the i th and k th particles ($v_i > v_k$) produces particles of an intermediate volume,

$$v_{i,k} = v_i + v_k. \quad (31)$$

To satisfy the conservations of the mass and the particle numbers at the same time, we partition this intermediate-volume particle into the two volume bins,

v_l and v_{l+1} ($v_l < v_{i,k} < v_{l+1}$), with fractions γ_l and γ_{l+1} , respectively. Unless v_l is the largest volume bin, these fractions can be written as

$$\gamma_l = \frac{v_{l+1} - v_{i,k}}{v_{l+1} - v_l} \quad (32)$$

and

$$\gamma_{l+1} = 1 - \frac{v_{l+1} - v_{i,k}}{v_{l+1} - v_l}. \quad (33)$$

If v_l is the largest volume bin, we cannot partition the intermediate particle but just put it into the largest volume bin v_{l+1} , although the mass conservation is not satisfied. We specify the volume ratio of two adjacent bins in § 2.5.

2.2.2. Monomer production rate

As described above, we assume that monomers are formed in situ from the precursor molecules HCN and C_2H_2 . Thus, we calculate the vertical profile of the mass production rate of monomers according to the distribution of the two molecules. We consider that the mass production rate of monomers, which means the total mass of monomers produced per unit volume per unit time, at altitude z is given by

$$p(v_1, z) = \frac{[f_{\text{HCN}}(z) + f_{\text{C}_2\text{H}_2}(z)] N(z)}{\int_0^\infty [f_{\text{HCN}}(z') + f_{\text{C}_2\text{H}_2}(z')] N(z') dz'} \dot{M}, \quad (34)$$

where f_{HCN} and $f_{\text{C}_2\text{H}_2}$ are the volume mixing ratios of HCN and C_2H_2 , respectively, and \dot{M} is the total mass production rate of monomers throughout the atmosphere and its physical unit is mass/area/time.

We assume that \dot{M} is proportional to the incident stellar Lyman-alpha ($\text{Ly}\alpha$) flux at the planet's orbital distance, $I_{\text{Ly}\alpha}$, because monomer production is relevant to UV photodissociation. Thus, we assume the photochemistry of monomer formation to be driven entirely by $\text{Ly}\alpha$. For the reference, we use the observed values of the incident solar $\text{Ly}\alpha$ flux, $I_{\text{Ly}\alpha, \text{Titan}}$, and mass production rate, \dot{M}_{Titan} , in the present Titan's atmosphere; namely,

$$\dot{M} = \beta \frac{I_{\text{Ly}\alpha}}{I_{\text{Ly}\alpha, \text{Titan}}} \dot{M}_{\text{Titan}}. \quad (35)$$

This is a simpler version of Eq. (8) of Trainer et al. (2006), which they derived empirically. Although both linear and quadratic dependences of \dot{M} on $I_{\text{Ly}\alpha}$ are proposed, there is still room for discussion to determine which relationship is appropriate (Trainer et al. 2006). The linear relationship would be valid when haze monomers are produced predominantly by photodissociation of hydrocarbon intermediate molecules, which is the product of photodissociation of CH_4 , while the quadratic relationship would be valid when haze monomers are produced mainly by thermochemical reactions between multiple intermediates (see Trainer et al.

(2006) for details). Because the relationship is totally uncertain for exoplanet atmospheres, we have adopted the linear relationship for simplicity, and added a numerical parameter β in the above equation. We adopt $1 \times 10^{-14} \text{ g cm}^{-2} \text{ s}^{-1}$ for \dot{M}_{Titan} , since microphysical models, photochemical models, and laboratory simulations all imply that the production rate of the monomers on Titan is in the range between 0.5×10^{-14} and $2 \times 10^{-14} \text{ g cm}^{-2} \text{ s}^{-1}$ (McKay et al. 2001). Also, we use $6.2 \times 10^9 \text{ photons cm}^{-2} \text{ s}^{-1}$ for $I_{\text{Ly}\alpha, \text{Titan}}$ (Trainer et al. 2006). When we vary β , we also vary the intensities of the actinic flux at all the wavelengths according to β (i.e., the $\text{Ly}\alpha$ intensity).

Finally, the boundary conditions for Eq. (11) are given as follows. As the lower boundary conditions, we consider that all the particles are lost with the larger of the sedimentation velocity and the downward velocity imposed by the atmospheric mixing, following Lavvas et al. (2010). As the upper boundary conditions, we set zero fluxes for all the particle sizes.

2.2.3. Calculation method

We divide the atmosphere into layers with the same thickness Δz and discretize Eq. (11) as

$$\begin{aligned} \frac{\partial n_j(v_i)}{\partial t} = & \frac{1}{2} \sum_{k=1}^{i-1} K_j(v_k, v_i - v_k) n_j(v_k) n_j(v_i - v_k) \\ & - n_j(v_i) \sum_{k=1}^{\mathcal{N}} K_j(v_i, v_k) n_j(v_k) \\ & - \frac{\Phi_{j+1/2}(v_i) - \Phi_{j-1/2}(v_i)}{\Delta z} + p_j(v_i), \quad (36) \end{aligned}$$

where the subscript j represents the physical quantities in the j th layer. We set the pressure at the mid-point altitude of the lowest layer as the lower boundary pressure. For Eq. (12), we use the upwind difference scheme instead of the central difference scheme for the calculation of sedimentation flux, because of numerical stability, and approximate $\Phi_{j+1/2}(v_i)$ as

$$\begin{aligned} \Phi_{j+1/2}(v_i) = & -V_{s,i,j+1} n_{j+1}(v_i) \\ & - K_{zz} N_{j+1/2} \frac{n_{j+1}(v_i) / N_{j+1} - n_j(v_i) / N_j}{\Delta z}. \quad (37) \end{aligned}$$

To obtain a steady-state solution, we solve the continuity Eq. (36) implicitly with the same solver DLSODES (Hindmarsh 1982) that we use in the photochemical calculations (§ 2.1). We adopt the values of relative (RTOL) and absolute (ATOL) tolerances as 10^{-4} and 10^{-20} , respectively. The initial number densities of all the sizes are set to zero. We adopt the criteria of convergence such that the volume-averaged sizes of particles in

all the layers, which we calculate as

$$s_{\text{vol}} = \frac{\sum_{i=1}^{\mathcal{N}} n(s_i) s_i^4}{\sum_{i=1}^{\mathcal{N}} n(s_i) s_i^3}, \quad (38)$$

are different by less than 1%.

2.3. Opacity

2.3.1. Haze particles

We calculate the extinction cross sections of haze particles based on the Mie theory (Mie 1908). In the limit where the particle radius, s , is large compared to the radiation wavelength, λ , the Mie theory agrees with geometric optics. On the other hand, the Mie theory reduces to the Rayleigh theory in the limit of $s \ll \lambda$.

From the Mie theory, the extinction cross section of a homogeneous spherical particle of radius s , σ_{ext} , can be written as (Bohren & Huffman 2004)

$$\sigma_{\text{ext}} = \pi s^2 \frac{2}{x^2} \sum_{n=1}^{\infty} (2n+1) \text{Re}(a_n + b_n), \quad (39)$$

where Re denotes the real part. Here, x is the size parameter defined as

$$x \equiv \frac{2\pi s}{\lambda}. \quad (40)$$

Coefficients a_n and b_n are calculated as

$$a_n = \frac{m\phi_n(mx)\phi'_n(x) - \phi_n(x)\phi'_n(mx)}{m\phi_n(mx)\zeta'_n(x) - \zeta_n(x)\phi'_n(mx)}, \quad (41)$$

and

$$b_n = \frac{\phi_n(mx)\phi'_n(x) - m\phi_n(x)\phi'_n(mx)}{\phi_n(mx)\zeta'_n(x) - m\zeta_n(x)\phi'_n(mx)}, \quad (42)$$

where m is the ratio of the complex refractive indices of the particle to the surrounding atmosphere. ϕ and ζ are the so-called Ricatti-Bessel functions and the prime indicates differentiation with respect to the argument in parentheses.

We use the `bhmie` code (Bohren & Huffman 2004) to calculate Eqs. (39)-(42). Complex refractive indices of haze are taken from Khare et al. (1984), which reports laboratory experiment results for production of tholin hazes in a simulated Titan's atmosphere (0.9 N₂/0.1 CH₄ gas mixture at 0.2 mb).

In Figure 1, we show the extinction cross sections of the haze particles of five different particle sizes, namely, 0.001 μm , 0.01 μm , 0.1 μm , 1 μm , and 10 μm . When the particle size is sufficiently small relative to the wavelength, the scattering is approximated by the Rayleigh scattering. More specifically, the cross sections for $s = 0.001 \mu\text{m}$, 0.01 μm , and 0.1 μm show the behavior due to the Rayleigh scattering in the visible wavelength region; namely, $\sigma_{\text{ext}} \propto \lambda^{-4}$. Also, the dependence on the particle radius is such that $\sigma_{\text{ext}} \propto s^3$ (e.g., Petty 2006). In contrast, for larger particles of 1 μm and 10 μm , no

such feature is found, and the cross sections are relatively independent of wavelength. Note that the bumps found around 3.0 μm and 4.6 μm come from the vibrational transitions of the C-H bond and C \equiv N bond of the tholin-like haze particles, respectively (Khare et al. 1984).

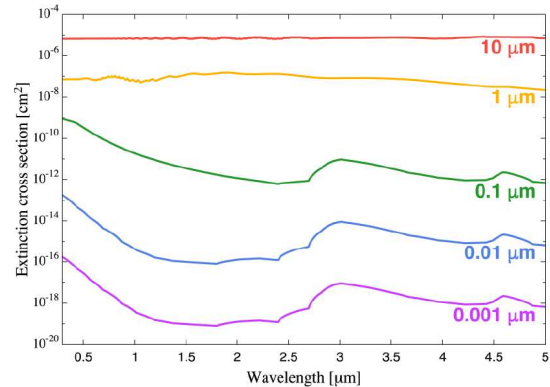


Figure 1. Extinction cross sections of the tholin-like haze particles of five different particle sizes of 0.001 μm , 0.01 μm , 0.1 μm , 1 μm , and 10 μm .

2.3.2. Gaseous species

For another source of radiative extinction in the atmosphere, we consider line absorption by H₂O, CO₂, CO, CH₄, O₂, NH₃, OH, N₂, HCN, C₂H₂, and H₂. We ignore the extinction by Na and K because they condense as Na₂S and KCl clouds, respectively, and settle downward in a temperature range of interest ($\lesssim 1000$ K) (Morley et al. 2013).

The extinction cross section of species i , at wavenumber ν , $\sigma_i(\nu)$, is written as

$$\sigma_i(\nu) = \sum_{\eta, \eta'} \sigma_{i, \eta \eta'}(\nu) \quad (43)$$

where $\sigma_{i, \eta \eta'}$ is the line absorption cross section for the transition from lower state η to upper state η' .

For briefly, we omit the subscript i hereafter. The line absorption cross section, $\sigma_{\eta \eta'}$, is given as

$$\sigma_{\eta \eta'}(\nu) = S_{\eta \eta'}(T) f(\nu - \nu_{\eta \eta'}), \quad (44)$$

where $\nu_{\eta \eta'}$ is the spectral line transition wavenumber, $S_{\eta \eta'}$ is the spectral line intensity, and f is the line profile function. We calculate $\sigma_{\eta \eta'}$, using the line data from HITRAN2012 (Rothman et al. 2013). When summing the absorption cross section for each transition, we do not consider the cross sections whose spectral line intensities are less than 10^{-40} cm^{-2} because of the computational cost.

According to Sharp & Burrows (2007) and Rothman et al. (1998), the spectral line intensity

at temperature T , $S_{\eta\eta'}(T)$, is written as

$$S_{\eta\eta'}(T) = \frac{\pi e^2 g_\eta f_{\eta\eta'} \exp(-hcE_\eta/k_B T)}{m_e c Q(T)} [1 - \exp(-hc(E_{\eta'} - E_\eta)/k_B T)] \quad (45)$$

$$= S_{\eta\eta'}(T_{\text{ref}}) \frac{Q(T_{\text{ref}}) \exp(-hcE_\eta/k_B T)}{Q(T) \exp(-hcE_\eta/k_B T_{\text{ref}})} \frac{[1 - \exp(-hc(E_{\eta'} - E_\eta)/k_B T)]}{[1 - \exp(-hc(E_{\eta'} - E_\eta)/k_B T_{\text{ref}})]}, \quad (46)$$

where g_η is the statistical weight of the lower state η , $f_{\eta\eta'}$ is the oscillator strength for the transition between the lower and upper states, E_η and $E_{\eta'}$ are the lower-state and upper-state energy, respectively, and $Q(T)$ is the total internal partition function at temperature T . e is the elementary charge, m_e is the electron mass, and h , c , and k_B are the Planck constant, the speed of light, and the Boltzmann constant, respectively. $S_{\eta\eta'}(T_{\text{ref}})$ is the spectral line intensity at the reference temperature T_{ref} and written as

$$S_{\eta\eta'}(T_{\text{ref}}) = \frac{\pi e^2 g_\eta f_{\eta\eta'} \exp(-hcE_\eta/k_B T_{\text{ref}})}{m_e c Q(T_{\text{ref}})} [1 - \exp(-hc(E_{\eta'} - E_\eta)/k_B T_{\text{ref}})]. \quad (47)$$

The HITRAN2012 database provides the values of E_η , $E_{\eta'}$, $S_{\eta\eta'}(T_{\text{ref}})$, and $Q(T_{\text{ref}})$, where $T_{\text{ref}} = 296\text{K}$. We calculate $Q(T)$ with the total internal partition sums (TIPS) code (Fischer et al. 2003) in the HITRAN database. This code calculates $Q(T)$ for given temperature (the temperature range is 70-3000 K) and molecular species in the HITRAN database.

We consider the air-broadened pressure-shift in the following way. The shifted spectral line transition wavenumber $\nu_{\eta\eta'}^*$ can be written as

$$\nu_{\eta\eta'}^* = \nu_{\eta\eta'} + \delta(P_{\text{ref}}) P, \quad (48)$$

where $\delta(P_{\text{ref}})$ is the air-broadened pressure shift, provided that the shift, $\delta(P_{\text{ref}})$, is small relative to $\nu_{\eta\eta'}$. Here, P_{ref} is the reference pressure. The HITRAN2012 database provides the values of $\delta(P_{\text{ref}})$, which we use in calculating the line absorption cross sections.

As for line broadening, we consider pressure broadening and Doppler broadening. The line profile for pressure broadening is given by the Lorentz profile (Petty 2006),

$$f_L(\nu - \nu_{\eta\eta'}) = \frac{\Gamma_P}{\pi [(\nu - \nu_{\eta\eta'})^2 + \Gamma_P^2]}, \quad (49)$$

where Γ_P is the line half width of the pressure broadening. On the other hand, the line profile for Doppler broadening is given by the Gaussian profile (Petty 2006),

$$f_D(\nu - \nu_{\eta\eta'}) = \frac{1}{\Delta\nu_D \pi^{1/2}} \exp\left[-\frac{(\nu - \nu_{\eta\eta'})^2}{\Delta\nu_D^2}\right], \quad (50)$$

where ν_D is the line half width of the Doppler broadening.

To consider both line profiles, the convolution of the Lorentz and Gaussian profiles, which is called the Voigt profile, is used:

$$f_V(\nu - \nu_{\eta\eta'}) = \int_{-\infty}^{\infty} f_L(\nu' - \nu_{\eta\eta'}) f_D(\nu - \nu') d\nu' \quad (51)$$

$$= \int_{-\infty}^{\infty} \frac{\Gamma_L}{\pi [(\nu' - \nu_{\eta\eta'})^2 + \Gamma_L^2]} \frac{1}{\Delta\nu_D \pi^{1/2}} \exp\left[-\frac{(\nu - \nu')^2}{\Delta\nu_D^2}\right] d\nu' \quad (52)$$

$$= \frac{1}{\Delta\nu_D \pi^{1/2}} \mathcal{H}\left(\frac{\Gamma_L}{\Delta\nu_D}, \frac{\nu - \nu'}{\Delta\nu_D}\right), \quad (53)$$

where $\mathcal{H}(a, y)$ is called the Voigt function and defined as

$$\mathcal{H}(a, y) \equiv \frac{a}{\pi} \int_{-\infty}^{\infty} \frac{e^{-x^2}}{(y-x)^2 + a^2} dx. \quad (54)$$

For the calculation of the Voigt function, we use the polynomial expansion of this function (Kuntz 1997; Ruyten 2004). We adopt any cut-off in the line wings.

In the HITRAN2012 database, the line half width of the pressure broadening is calculated as

$$\Gamma_P(P, T) = \left(\frac{T_{\text{ref}}}{T}\right)^n [\Gamma_{\text{air}}(P_{\text{ref}}, T_{\text{ref}})(P - P_s) + \Gamma_{\text{self}}(P_{\text{ref}}, T_{\text{ref}})] \quad (55)$$

where Γ_{air} and Γ_{self} are, respectively, the air-broadened halfwidth and the self-broadened halfwidth at half maximum (HWHM) at $T_{\text{ref}} = 296\text{K}$ and $P_{\text{ref}} = 1\text{atm}$ and P_s is the partial pressure. The line half width of the Doppler broadening is given by

$$\Delta\nu_D = \nu \left(\frac{2kT}{mc^2}\right)^{1/2}, \quad (56)$$

where m is the mass of the molecule (Petty 2006).

We also consider the Rayleigh scattering by those molecules except OH and the collision-induced absorption by H₂-H₂ and H₂-He. We have confirmed that the Rayleigh scattering by OH is negligible for the total extinction by all the molecules because of its low abundance in the atmosphere. The Rayleigh scattering cross section is given by (Liou 2002)

$$\sigma_{\text{Rayleigh}} = \frac{128\pi^5}{3\lambda^4} \alpha^2, \quad (57)$$

where α is the polarizability. We use the value of the polarizability for each molecule from CRC Handbook of CHEMISTRY and PHYSICS (Haynes 2012). The collision-induced absorption cross sections are taken from HITRAN2012 (Rothman et al. 2013).

2.4. Transmission Spectrum Model

We model transmission spectra following [Brown \(2001\)](#). The transit depth at wavelength λ , $D(\lambda)$, can be defined as

$$D(\lambda) = \frac{L_s(\lambda) - L_{\text{obs}}(\lambda)}{L_s(\lambda)}. \quad (58)$$

Here, L_s is the disk-integrated luminosity from the host star given by

$$L_s(\lambda) = \int_0^{R_s} F_s(\lambda) 2\pi r dr, \quad (59)$$

where R_s and F_s are the stellar radius and flux, respectively, and r is the impact parameter measured from the disk center. L_{obs} is the disk-integrated luminosity of the host star during transit. Here, we assume that the incident stellar light rays are parallel and thus F_s is constant through the stellar disk, because the orbital distances of planets of interest are much larger (by a factor of 10-100) than the host star's radius. With this assumption, L_{obs} is expressed as

$$L_{\text{obs}}(\lambda) = \int_0^{R_s} F_s(\lambda) e^{-\tau(r,\lambda)} 2\pi r dr, \quad (60)$$

where $\tau(r, \lambda)$ is the so-called chord optical depth defined by

$$\tau(r, \lambda) = 2 \int_0^\infty \sum_{i=1}^{\mathcal{N}} \sigma_i(r, s, \lambda) N_i(r, s) ds. \quad (61)$$

Here, σ_i and N_i are the extinction cross section and number density of species i , \mathcal{N} is the number of species whose extinction is considered, and ds is the line element along the line of sight.

In this study, we assume that all the parts inside the sphere of radius R_0 are optically thick enough to block the incident stellar light completely. The radius R_0 may be defined as that of a solid surface or an optically thick cloud deck in the atmosphere, if present. However, some exoplanets may have no such well-defined boundary. Even if there is such a boundary, its radius is unknown in advance. According to our numerical results, τ is sufficiently larger than unity below the pressure level of 10 bar in the atmosphere considered in this study. Thus, we define R_0 as the radial distance from the planetary center at which the pressure is 10 bar.

With the above assumption and from Eqs. (58) to (60), the transit depth $D(\lambda)$ can be written as

$$D(\lambda) = \frac{R_0^2 + \int_{R_0^2}^{R_s^2} [1 - e^{-\tau(r,\lambda)}] dr^2}{R_s^2}. \quad (62)$$

The so-called transit radius, $R_{\text{tr}}(\lambda)$, is defined as

$$R_{\text{tr}}(\lambda) \equiv R_s \sqrt{D(\lambda)}. \quad (63)$$

2.5. Calculation Procedure and Model Parameters

Finally, we summarize the calculation procedure and the model parameters and their values that we use in our simulations.

First, we derive the vertical profiles of volume mixing ratios of the gaseous species, f_i , from the photochemical calculations (§ 2.1). Then, from the sum of f_{HCN} and $f_{\text{C}_2\text{H}_2}$, which corresponds to the distribution of the haze precursors, we simulate the particle growth and calculate the number density distribution of each haze volume $n(v_i, z)$ (§ 2.2). After that, with the obtained size and number density distributions of haze particles and the vertical distribution of the gaseous species, we model transmission spectrum of the atmosphere (§ 2.4) with calculations of opacities of gaseous species and haze particles (§ 2.3). The opacity and transit depth is calculated every wavenumber grid with width of 0.1 cm^{-1} .

In this study, we model the transmission spectra assuming the properties of the super-Earth GJ 1214b. Among super-Earths found so far, the atmosphere of GJ 1214b has been probed most by transit observations at multiple wavelengths. The model parameters and their values we use are listed in Table 1. We will explore dependence of results on model parameters other than monomer production rate such as metallicity, C/O ratio, eddy diffusion coefficient, atmospheric temperature profile, and monomer size in our forthcoming papers.

We adopt the value of the radius at the 1000-bar pressure level (simply called the 1000-bar radius, hereafter) as $2.07 R_\oplus$, which is 74% of the planet radius reported by [Anglada-Escudé et al. \(2013\)](#); We have found that this value of the 1000-bar radius can roughly match the observed transit radii of GJ 1214b when we assume a clear solar composition atmosphere. Note that when we infer the molecular abundance from observational transmission spectrum, we suffer from degeneracy among the reference radius, 1000-bar radius, and inferred molecular abundance (see [Heng & Kitzmann 2017](#)).

For the temperature-pressure profile, we use the analytical formula of [Guillot \(2010\)](#), because its smooth and simple function suits computationally-heavy photochemical calculations. With Eq. (29) of [Guillot \(2010\)](#), we calculate the temperature-pressure profile averaging over the whole planetary surface (i.e., $f = 1/4$ in the equation). We choose the parameters, namely, the intrinsic temperature T_{int} , equilibrium temperature T_{irr} , averaged opacity in the optical k_v , and averaged opacity in the infrared k_{th} , so as to match the temperature-pressure profile of GJ 1214b that [Miller-Ricci & Fortney \(2010\)](#) derived for a solar composition atmosphere under the assumption of efficient heat redistribution from the day and night sides. This yields $T_{\text{int}} = 120 \text{ K}$, $T_{\text{irr}} = 790 \text{ K}$, $k_v = 10^{-4.0} \text{ g cm}^{-2}$, and $k_{\text{th}} = 10^{-2.6} \text{ g cm}^{-2}$.

We have confirmed that our profile agrees with that of [Miller-Ricci & Fortney \(2010\)](#) within 86 K for the grids we adopt. We adopt the value of eddy diffusion coefficient K_{zz} as $1 \times 10^7 \text{ cm}^2 \text{ s}^{-1}$. We will explore the sensitivity of transmission spectrum to eddy diffusion coefficient in our forthcoming papers. As for the elemental abundance ratios, we assume that of the solar system abundance, which we take from Table 2 of [Lodders \(2003\)](#), corresponding to C/O, O/H, and N/H of 5.010×10^{-1} , 5.812×10^{-4} , and 8.021×10^{-5} , respectively.

As for the stellar spectrum used in the photochemical model, we use that of GJ 1214 constructed by the MUSCLES Treasury Survey ([France et al. 2016](#); [Youngblood et al. 2016](#); [Lloyd et al. 2016](#)), the wavelength coverage of which is from 0.55 nm to 5500 nm. The spectrum for X-rays is constructed from Chandra/XMM-Newton and APEC models ([Smith et al. 2001](#)), that for EUV from empirical scaling relation based on Ly α flux ([Linsky et al. 2014](#)), that for Ly α from model fit to line wings ([Youngblood et al. 2016](#)), and that for visible-IR from synthetic photospheric spectra from PHOENIX atmosphere models ([Husser et al. 2013](#)). We use the version 1.1 of the panchromatic SED binned to a constant 1 Å resolution and downsampled in low signal-to-noise regions to avoid negative flux, the data of which is taken from the MUSCLES team’s website⁴. We adopt 1 angstrom as the spectral resolution we use. The Ly α flux of GJ 1214, which is located at 14.6 pc far away from the Sun, was observed as $1.3_{-0.5}^{+1.4} \times 10^{-14} \text{ erg cm}^{-2} \text{ s}^{-1}$ at the Earth ([Youngblood et al.](#)

[2016](#)). From this value, we calculate the Ly α flux at the planet’s orbit as $3.3 \times 10^{13} \text{ photons cm}^{-2} \text{ s}^{-1}$ using the value of GJ 1214b’s semi-major axis, 0.0148 AU ([Anglada-Escudé et al. 2013](#)), and the Ly α wavelength of 121.6 nm. Note that when considering the effects of the mass production rate of haze monomers (i.e., the Ly α flux), we vary the intensities of the actinic flux at all the wavelengths according to the Ly α intensity.

As for the monomer radius s_1 , we adopt $1 \times 10^{-3} \mu\text{m}$. We prepare 40 volume bins, setting the volume ratio of two adjacent bins to be 3 ([Lavvas et al. 2010](#)), and cover from $1 \times 10^{-3} \mu\text{m}$ (monomer size) to 1600 μm . As for the value of haze particle internal density ρ_p , we adopt 1.0 g cm^{-3} , which is adopted by most of the particle growth models for hydrocarbon hazes in Titan’s atmosphere (e.g. [Toon et al. 1992](#); [Lavvas et al. 2010](#)).

In the photochemical calculations, the atmosphere is vertically divided into 165 layers with thickness of 45 km, placing the lower boundary pressure at 1000 bar. This thickness is sufficiently smaller relative even to the minimum atmospheric scale height in the atmosphere, which is 177 km. In the case of the particle growth model, we consider the pressure range from 10 bar to 10^{-10} bar with 200 same thickness layers.

Simplified version of our transmission spectrum models are used for WASP-80b in [Fukui et al. \(2014\)](#) and for HAT-P-14b in [Fukui et al. \(2016\)](#). In the spectrum models of [Fukui et al. \(2014\)](#), we ignored the photochemical reactions and regarded the particle size, particle number density, altitude and thickness of the haze layer as input parameters. In [Fukui et al. \(2016\)](#), we did not consider the effects of haze on the spectra.

Table 1. Model parameters and their values used in the simulations

Parameter	Description	Value	Reference
R_s	Host star radius	$0.201 R_\odot$	Anglada-Escudé et al. (2013)
M_p	Planet mass	$6.26 M_\oplus$	Anglada-Escudé et al. (2013)
$R_{1000 \text{ bar}}$	1000-bar radius	$2.07 R_\oplus$	
K_{zz}	Eddy diffusion coefficient	$1.00 \times 10^7 \text{ cm}^2 \text{ s}^{-1}$	
s_1	Monomer radius	$1.00 \times 10^{-3} \mu\text{m}$	
ρ_p	Particle internal density	1.00 g cm^{-3}	
$I_{\text{Ly}\alpha}$	Ly α flux at the planet’s orbit	$3.30 \times 10^{13} \text{ photons cm}^{-2} \text{ s}^{-1}$	Youngblood et al. (2016)

3. RESULTS

In this section, we show results of our numerical simulations. First, we investigate the fiducial monomer production case (i.e., $\beta = 1$) in § 3.1-3.3 and then explore the dependence on the monomer production rate

⁴ <https://archive.stsci.edu/prepds/muscles/>

by changing β in § 3.4.

3.1. Photochemical Calculations

First we outline the photochemistry of the atmosphere. Although the results we show below are basically the same as those from the previous studies, we show them because they are helpful in interpreting our later results. We note that our photochemical models of GJ 1214b’s atmosphere are the first ones that use the observed GJ 1214’s UV spectrum (France et al. 2016; Youngblood et al. 2016; Loyd et al. 2016).

Figure 2 shows the calculated vertical distributions of gaseous species in the photochemical equilibrium state (solid lines). We also present the distributions obtained by thermochemical equilibrium calculations (dashed lines) that ignore photochemical processes and eddy diffusion. In the lower atmosphere ($P \gtrsim 10^{-4}$ bar), the eddy diffusion mixing, which tends to smooth out compositional gradients, is found to yield constant abundances of H_2O , CH_4 , NH_3 , N_2 , and CO equal to the lower boundary values. In the upper atmosphere ($P \lesssim 10^{-4}$ bar), it turns out that many species (i.e., H, O, C, HCN, N, O_2 , C_2H_2 , CH_3 , OH, CH_3OH , NH_2 , CH_2 , and $\text{O}(^1\text{D})$) that are quite rare in thermochemical equilibrium states are produced photochemically and H is the most abundant species. The H is known to act as a reactive radical in reducing atmospheres (Hu et al. 2012).

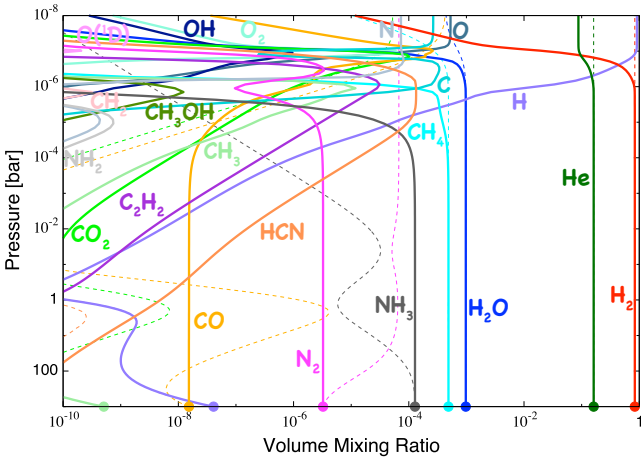


Figure 2. Vertical distributions of gaseous species in the photochemical equilibrium atmosphere. Filled circles represent the thermochemical equilibrium values at the lower boundary. The thermochemical equilibrium abundances are shown with dashed lines for reference. Note that the eddy diffusion transport is not included in the thermochemical equilibrium calculations.

As for the haze precursors, HCN and C_2H_2 , f_{HCN} is always greater than $f_{\text{C}_2\text{H}_2}$. This means that in our simulations, the profile of the production rate of monomers is determined mainly by that of f_{HCN} . The ratio f_{HCN} is constant in the pressure range of 1×10^{-6} bar to

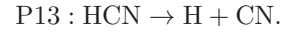
1×10^{-5} bar because HCN is the most stable N-bearing species in this range.

The details of the production and loss mechanisms of HCN and C_2H_2 was discussed in Moses et al. (2011) for the cases of two hot Jupiters, HD 189733b and HD 209458b. Nevertheless, below, we also explore how the steady-state abundances of HCN and C_2H_2 are maintained, since the atmospheric temperature considered in this study is lower than HD 189733b ($T_{\text{eq}} = 1100$ K) and HD 209458b ($T_{\text{eq}} = 1316$ K⁵).

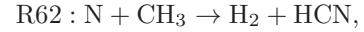
In Figure 3, we plot the distributions of the production and loss rates of HCN due to thermochemical and photochemical reactions, and transport by eddy diffusion for the steady-state distribution of HCN. In the pressure range of 1×10^{-7} bar to 3×10^{-6} bar, the steady-state is maintained almost by the production process via the thermochemical reaction,



and the loss process via photodissociation,

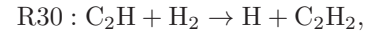


On the other hand, in the pressure range of 3×10^{-6} bar to 2×10^{-3} bar, the steady-state is maintained by a balance between the production process via the thermochemical reaction,

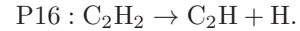


and the loss process via eddy diffusion transport to the upper atmosphere.

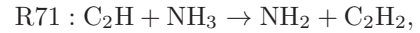
Figure 4 is the same as Fig. 3 but for C_2H_2 . In the pressure range of 1×10^{-7} bar to 5×10^{-6} bar, the steady-state is determined by the production process via the thermochemical reaction,



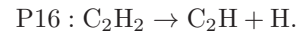
and the loss process via photodissociation,



On the other hand, in the pressure range of 5×10^{-6} bar to 2×10^{-5} bar, the steady-state is determined by production process via the thermochemical reaction,



and the loss process, via photodissociation,



3.2. Particle Growth Calculations

The growth of haze particles occurs via competition among coagulation, sedimentation, and diffusion.

⁵ <http://www.openexoplanetcatalogue.com>

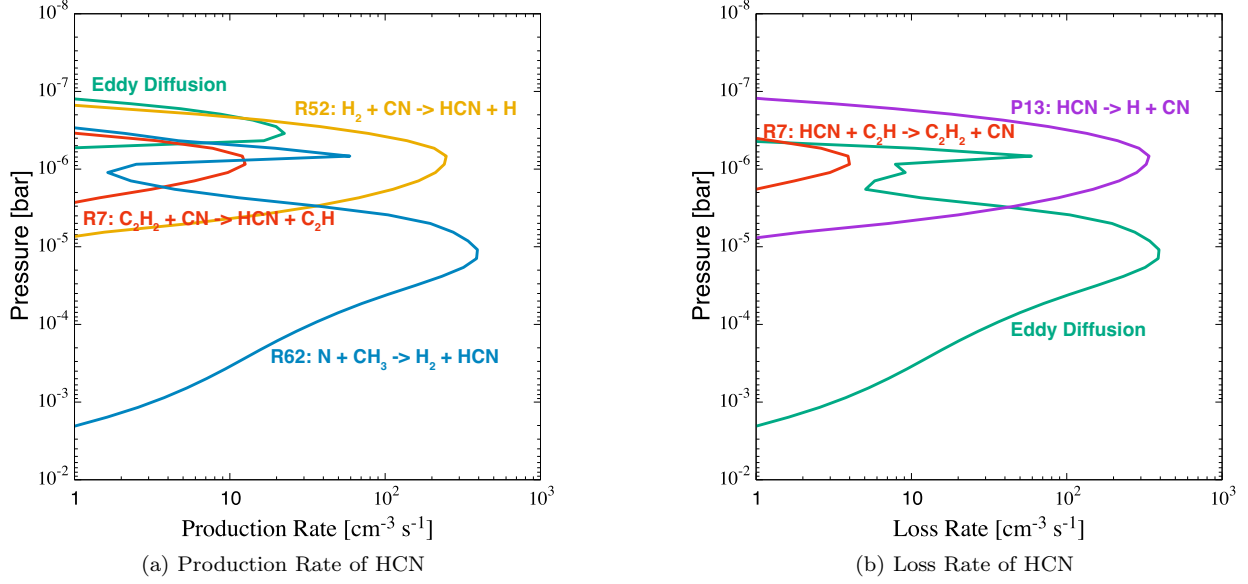


Figure 3. Distributions of (a) the production and (b) loss rates of HCN due to thermochemical and photochemical reactions, and transport by eddy diffusion for the steady-state distribution of HCN.

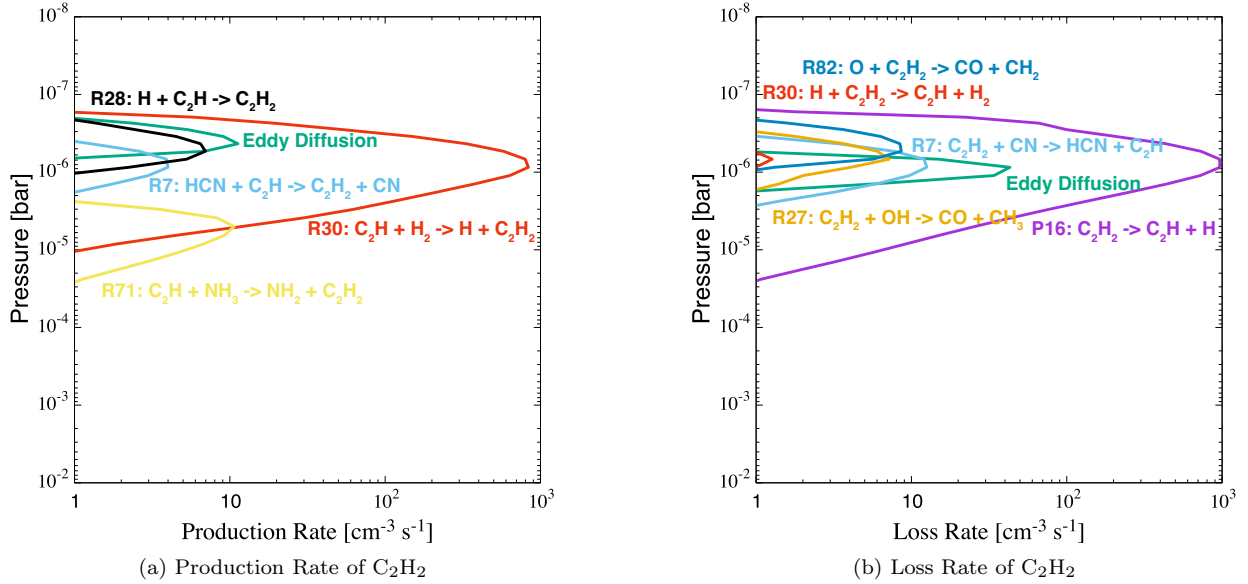


Figure 4. Distributions of (a) the production and (b) loss rates of C₂H₂ due to thermochemical and photochemical reactions, and transport by eddy diffusion for the steady-state distribution of C₂H₂.

Knowledge of the sedimentation velocity is therefore helpful in understanding the particle growth. Figure 5 shows the sedimentation velocity along pressure for five different particle radii, $1.0 \times 10^{-3} \mu\text{m}$, $3.9 \times 10^{-2} \mu\text{m}$, $1.5 \mu\text{m}$, $59 \mu\text{m}$, and $1600 \mu\text{m}$. Change of the trend found at $P \sim 10^{-2}$ bar for the $59 \mu\text{m}$ particle and $P \sim 10^{-3}$ bar for the $1600 \mu\text{m}$ particle, respectively, results from the transition from slip flow ($K_{n,i} = \lambda_a/s_i > 1$) to Stokes flow ($K_{n,i} = \lambda_a/s_i < 1$). In the slip flow regime, the sedimentation velocity is proportional to the particle radius (see Eqs. (13) and (17)). On the other hand,

in the Stokes flow regime, the sedimentation velocity is proportional to the square of the particle radius (see Eqs. (13) and (17)).

Figure 6 shows the vertical profiles of haze properties. Here, we define the surface average radius s_{surf} (yellow solid line) as

$$s_{\text{surf}} = \frac{\sum_{i=1}^{\mathcal{N}} n(s_i) s_i^3}{\sum_{i=1}^{\mathcal{N}} n(s_i) s_i^2}, \quad (64)$$

and the volume average radius s_{vol} (red solid line) by Eq. (38). If the two average sizes agree with each other

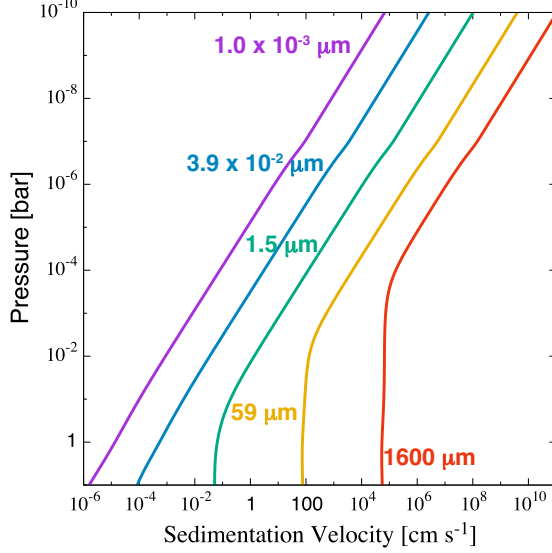


Figure 5. Sedimentation velocity for five different particle radii, $1.0 \times 10^{-3} \mu\text{m}$ (purple line), $3.9 \times 10^{-2} \mu\text{m}$ (blue line), $1.5 \mu\text{m}$ (green line), $59 \mu\text{m}$ (orange line), and $1600 \mu\text{m}$ (red line) along pressure.

at a certain altitude, the size distribution is unimodal at the altitude. The surface average number density n_{surf} (yellow dashed line) and the volume average number density n_{vol} (red dashed line) are calculated as

$$n_{\text{surf}} = \frac{\sum_{i=1}^{\mathcal{N}} n(s_i) s_i^3}{s_{\text{surf}}^3} \quad (65)$$

and

$$n_{\text{vol}} = \frac{\sum_{i=1}^{\mathcal{N}} n(s_i) s_i^3}{s_{\text{vol}}^3}, \quad (66)$$

respectively. Also, the mass densities for all the size bins at each pressure level are plotted with the blue color contour and the vertical profile of the monomer mass production rate is plotted with the green solid line.

From Fig. 6, it is demonstrated that the average radii change dramatically with altitude. In the upper atmosphere, particles grow little because they settle faster than coagulation proceeds. The number densities become larger as altitude decreases (or the pressure increases) and they take the peak value at $P \sim 10^{-7}$ bar. Coagulation growth occurs significantly below this pressure level. As altitude decreases, the average radii increase from $1 \times 10^{-3} \mu\text{m}$ to $2\text{--}3 \mu\text{m}$ because of coagulation growth, and the number densities decrease by several orders of magnitude from the peak values. Again, change of the trend found at $P \sim 10^{-2}$ bar results from the transition from the slip flow to Stokes flow regimes. A significant increase in the sedimentation velocity due to the regime transition of drag force (see Fig. 5) inhibits the collision between particles.

The slight difference between s_{surf} and s_{vol} means that the haze contains different size particles at each altitude.

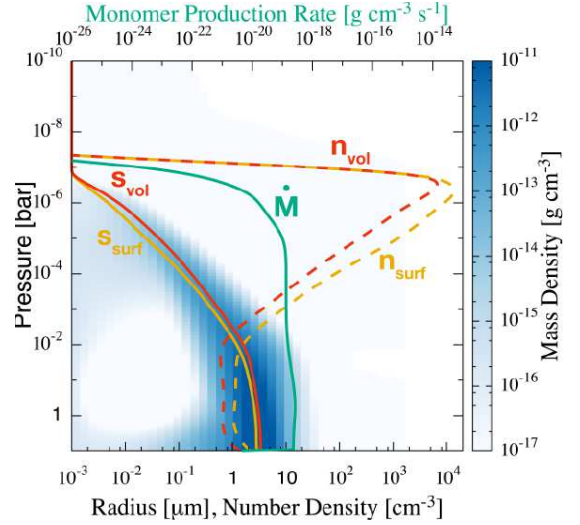


Figure 6. Vertical profiles of the surface average radius s_{surf} (yellow solid line) and number density n_{surf} (yellow dashed line) and the volume average radius s_{vol} (red solid line) and number density n_{vol} (red dashed line) along with that of the monomer mass production rate (green solid line). See the text for the definition of each quantity. Also, the mass densities for all the size bins at each pressure level are plotted with the blue color contour.

The color contour indicates that particles in some narrow range of size are abundant at each altitude and the monomer size particles exist broadly below the level of 10^{-7} bar because monomer production occurs in this region.

In Figure 7, we plot the distributions of number density of haze particles for all the size bins at seven different pressure levels, 3.4×10^{-8} bar, 2.3×10^{-7} bar, 8.3×10^{-6} bar, 4.9×10^{-4} bar, 3.7×10^{-2} bar, 0.95 bar, and 10 bar. First it is found that the number density of monomer size, $10^{-3} \mu\text{m}$, is the largest among all the sizes at all the pressure levels because of the large monomer production rate. At low pressures of $P \lesssim 10^{-5}$ bar, the coagulation due to brownian diffusion is the dominant process, whereas that due to gravitational collection hardly occurs. On the other hand, at high pressures of $P \gtrsim 10^{-5}$ bar, both coagulation mechanisms contribute to the particle growth. The coagulation due to gravitational collection makes a second peak of number density for the pressure levels higher than 8.3×10^{-6} bar, because it occurs in a runaway fashion much more rapidly compared to that due to brownian diffusion.

The change of size distribution can be understood as follows: The particles grow through the frequent collisions with the abundant small particles. The collision timescale τ_{coll} between a large particle and monomer size particles can be written as $\tau_{\text{coll}} = (n_1 \sigma \Delta v)^{-1}$, where n_1 is the number density of monomers, σ is the collision cross section of the large particle, and Δv is the relative

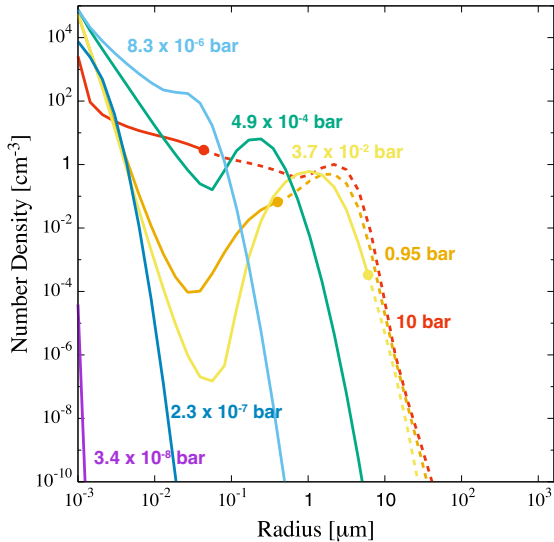


Figure 7. Distributions of number density of haze particles for all the size bins at seven different pressure levels, 3.4×10^{-8} bar (purple line), 2.3×10^{-7} bar (blue line), 8.3×10^{-6} bar (light blue line), 4.9×10^{-4} bar (green line), 3.7×10^{-2} bar (yellow line), 0.95 bar (orange line), and 10 bar (red line). The Stokes regime is indicated by dashed lines, while the slip flow regime is indicated by solid lines; the transition points are marked by filled circles.

velocity between the particles. The relative velocity due to sedimentation is proportional to particle radius s in the slip flow regime and s^2 in the Stokes flow regime (see Eqs. (13) and (17)), while the relative velocity due to brownian diffusion is proportional to $s^{-\frac{3}{2}}$ (see Eq. (22)). Thus, $\tau_{\text{coll}} \propto s^{-3}$ (slip flow) and $\propto s^{-4}$ (Stokes flow) for gravitational collection, while $\tau_{\text{coll}} \propto s^{-1/2}$ for brownian diffusion. This means the particle growth is always a runaway process: The larger the particle, the faster the growth proceeds. Also, the gravitational collection is much faster than the brownian diffusion especially for large size particles. Therefore, from $P \sim 10^{-5}$ bar on, the second peak grows rapidly and a valley-shaped distribution develops (see yellow and orange lines), because gravitational collection contributes predominantly to the particle growth above this pressure.

At $P = 10$ bar, however, the valley is found to disappear. This is because the drag law for the large particles shifts from the slip flow regime to the Stokes regime. In Fig 7, the Stokes regime is indicated by dashed lines, while the slip flow regime is indicated by solid lines; the transition points are marked by filled circles. Since the sedimentation velocity is so high in the Stokes regime (see Fig. 5) that the particles settle faster than they grow, the largest-size group ($\gtrsim 2 \mu\text{m}$) stops growing (see the orange lines). Then, small particles, which are still in the slip flow regime, grow and are catching up with the largest particles.

In Figure 8, we plot the distributions of mass density for all the size bins at the same set of seven different

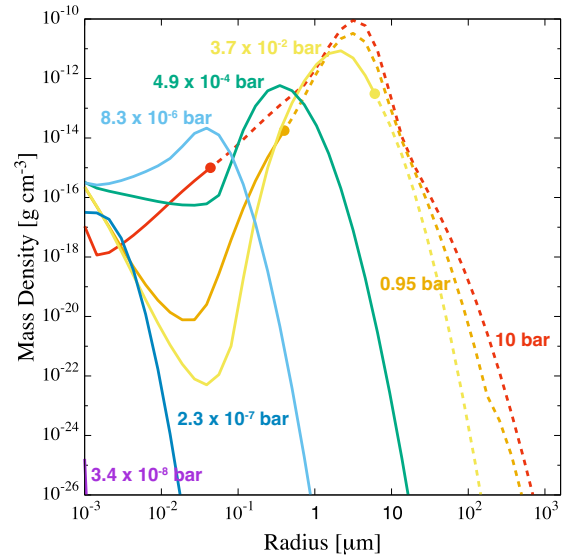


Figure 8. Same as Fig. 7 but the distribution of mass density.

pressure levels as shown in Fig. 7. It can be noticed that there are dominant sizes that account for most of the total haze mass for all the seven pressure levels. And the dominant size becomes larger, as pressure increases, because of the coagulative growth.

3.3. Transmission Spectrum Models

Figure 9 shows the transmission spectrum models for the atmosphere with haze (green line) and without haze (black line). Also, the relative cross section of the planetary disk with radius corresponding to a certain pressure level, which is defined as

$$D_P = \frac{R_P^2}{R_s^2}, \quad (67)$$

is presented by horizontal dotted lines from $P = 1 \times 10^{-6}$ bar to 1 bar for the atmosphere without haze. In equation (67), R_P and R_s are the radius at the pressure level P and the stellar radius, respectively. Roughly at these pressure levels, there exist the molecules accountable for the spectral features. We have confirmed that the chord optical depth at the pressure that corresponds to the transit radius is between 0.1 and 1, depending on wavelength. Note that the transmission spectrum models are smoothed for clarity by averaging over the nearest 633 wavenumber points, namely 63.2 cm^{-1} , for each point. We use the same smoothing method for the results of spectrum models hereafter.

In the spectrum model for the atmosphere without haze (black line), several characteristic spectral features can be seen. For example, prominent features of H_2O are found around $\lambda = 0.7 \mu\text{m}$, $0.8 \mu\text{m}$, $0.9 \mu\text{m}$, $1.2 \mu\text{m}$, $1.3\text{-}1.6 \mu\text{m}$, $1.9 \mu\text{m}$, and $2.5\text{-}3.0 \mu\text{m}$, those of CH_4 around $1.7 \mu\text{m}$, $2.2\text{-}2.4 \mu\text{m}$, and $3.3 \mu\text{m}$, and that of HCN

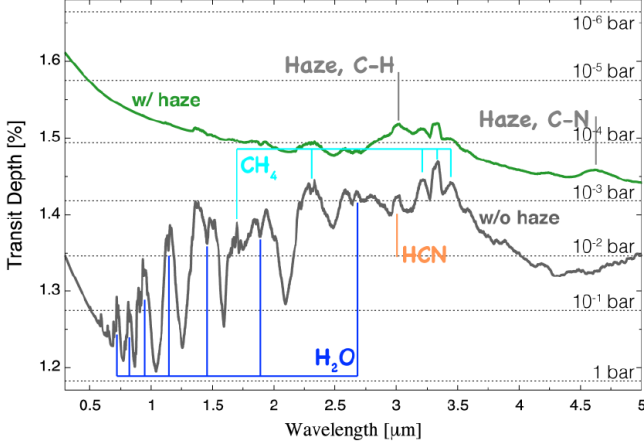


Figure 9. Transmission spectrum models for the atmosphere with haze (green line) and without haze (black line). Horizontal dotted lines represent the transit depths corresponding to the pressure levels from 1×10^{-6} bar to 1 bar for the atmosphere without haze. Note that the transmission spectrum models are smoothed for clarity by averaging over the nearest 633 wavenumber points, namely 63.2 cm^{-1} , for each point.

around $3.0 \mu\text{m}$. The Rayleigh scattering feature mainly due to H_2 can be seen in the optical wavelength region.

The spectrum for the atmosphere with haze (green line) is relatively featureless, compared to that for the atmosphere without haze (black line). This is because the haze particles in the upper atmosphere ($P \lesssim 10^{-4}$ bar) makes the atmosphere optically thick and prevent the molecules in the lower atmosphere ($P \gtrsim 10^{-4}$ bar) from showing their absorption features. However, the small features of CH_4 above 10^{-4} bar can be seen at $2.2\text{-}2.4 \mu\text{m}$ and $3.3 \mu\text{m}$ because of their large extinction cross sections at these wavelengths. Also, the spectral features due to the C-H and $\text{C}\equiv\text{N}$ bonds of the haze particles appear at 3.0 and $4.6 \mu\text{m}$, respectively.

In the wavelength region of $0.3\text{-}1 \mu\text{m}$ (green line), the spectral slope due to Rayleigh scattering by small ($\lesssim 0.1 \mu\text{m}$) haze particles in the upper atmosphere ($P \lesssim 10^{-4}$ bar) can be seen. Previous studies demonstrated that the existence of two separate cloud layers were needed to explain both the spectral slope in the optical and the lack of the absorption features in the near-infrared simultaneously; A layer composed of small size ($\lesssim 0.1 \mu\text{m}$) particles in the upper atmosphere responsible for the spectral slope due to Rayleigh scattering and the dense cloud layer that prevents the molecules from showing their absorption features (Ehrenreich et al. 2014; Sing et al. 2015; Dragomir et al. 2015). This study is the first to produce the transmission spectrum that has the spectral slope, but no distinct molecular absorption features, without assuming such cloud layers, by calculating the distribution of the size and number density of haze particles in

the atmosphere directly.

3.4. Dependence on Monomer Production Rate

Here, we explore the dependence of the transmission spectrum on monomer production rate \dot{M} by changing the haze monomer production parameter β (see Eq. (35)). As mentioned in § 2.5, when we vary the value of \dot{M} , we also vary the actinic flux at all the wavelengths according to the change in the incident stellar Ly α flux.

Figure 10 shows the calculated vertical distributions of gaseous species for four different values of β , (a) 10^5 , (b) $10^{2.5}$, (c) $10^{-2.5}$, and (d) 10^{-5} , respectively. We have confirmed the dependence of the molecular vertical distributions on the incident UV flux reported by previous works (e.g., Miguel & Kaltenegger 2014; Venot et al. 2014), as shown in Fig. 10. In the high UV cases ($\beta = 10^5$ and $10^{2.5}$), the photodissociation of the molecules such as H_2 , H_2O , CH_4 , and NH_3 occurs and produces H, O, C, HCN, N, O_2 , C_2H_2 , CH_3 , OH, $\text{O}(^1\text{D})$, and CH_3OH at deeper levels than in the fiducial case (Fig. 2). On the other hand, in the low UV cases ($\beta = 10^{-2.5}$ and 10^{-5}), the photodissociation does not occur effectively and the eddy diffusion evens out the abundance of the molecules such as H_2O , CH_4 , and NH_3 up to higher altitudes.

As for the haze precursors, HCN is always more abundant than C_2H_2 , irrespective of UV flux. Note that assumed values of C/O, O/H, and N/H are 5.010×10^{-1} , 5.812×10^{-4} , and 8.021×10^{-5} , respectively. It can be seen that the higher (lower) the incident UV flux is, the lower (higher) the region where the precursors are produced photochemically becomes, because of the effective photodissociation.

Figure 11 shows the vertical profiles of the surface average radius s_{surf} (yellow solid line) and number density n_{surf} (yellow dashed line), and the volume average radius s_{vol} (red solid line) and number density n_{vol} (red dashed line) along with that of the monomer mass production rate \dot{M} (green solid line) for four different values of β , (a) 10^5 , (b) $10^{2.5}$, (c) $10^{-2.5}$, and (d) 10^{-5} . The mass densities for all the size bins at each pressure level are also plotted with the blue color contour. The average radii are found to depend on the value of β dramatically: s_{vol} becomes as large as $10^3 \mu\text{m}$ in the case of $\beta = 10^5$, while it grows only to less than $1 \mu\text{m}$ in the case of $\beta = 10^{-5}$ at the lower boundary where the pressure is 10 bar. For the high UV cases ($\beta = 10^5$, and $10^{2.5}$), the disagreement between s_{surf} and s_{vol} is significantly larger compared to that in the fiducial case (Fig. 6) and one clearly finds bimodal distributions due to the large monomer production rate, as explained in detail below.

In Figure 12, we plot the distributions of number density for all the size bins at seven different pressure lev-

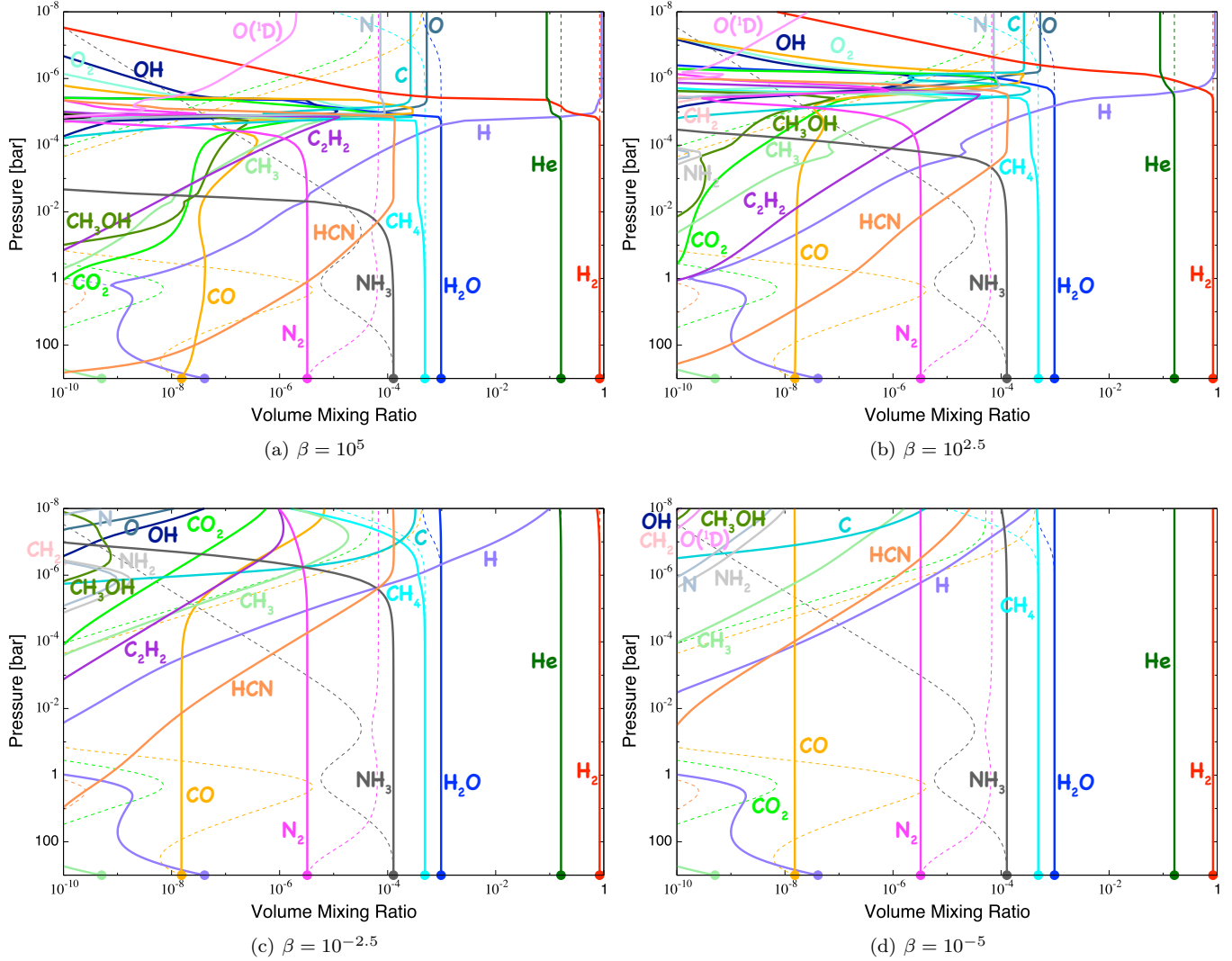


Figure 10. Same as Fig. 2 but for haze monomer production parameter $\beta =$ (a) 10^5 , (b) $10^{2.5}$, (c) $10^{-2.5}$, and (d) 10^{-5} . See Eq. (35) for the definition of β .

els, 3.3×10^{-8} bar, 2.3×10^{-7} bar, 8.7×10^{-6} bar, 4.7×10^{-4} bar, 3.9×10^{-2} bar, 0.90 bar, and 10 bar for the case of $\beta = 10^5$. Same as in Fig. 7, the slip flow and Stokes regimes are indicated by solid and dashed lines, respectively, and the transition points are marked by filled circles. First, similarly to the case of $\beta = 1$ (Fig. 7), the number density of the monomer size, $10^{-3} \mu\text{m}$, is the largest at all the pressure levels, because of the large monomer production rate. Like in the fiducial case, for $P \lesssim 10^{-5}$ bar, the coagulation due to brownian diffusion is the dominant process, whereas that due to gravitational collection hardly occurs. On the other hand, at high pressures of $P \gtrsim 10^{-5}$ bar, both coagulation mechanisms contribute to the particle growth. One finds a bimodal distribution with a wide gap whose center is around $40 \mu\text{m}$ for 3.9×10^{-2} bar, 0.90 bar, and 10 bar (note that the vertical range of Fig. 12 differs greatly

from that of Fig. 7). In contrast to the fiducial case, the particle growth proceeds rapidly as a whole and, then, the large-size particles ($\gtrsim 400 \mu\text{m}$) enter to the Stokes regime (see the green line) before development of any peak like ones observed in Fig. 7. Thus, the largest-size ($\gtrsim 400 \mu\text{m}$) group stops growing and the small particles in the slip flow regime ($40 \mu\text{m} \lesssim s \lesssim 400 \mu\text{m}$) grow and catch up with the largest ($\gtrsim 400 \mu\text{m}$) particles in the Stokes regime. However, in this case, even relatively small ($\lesssim 40 \mu\text{m}$) particles are already in the Stokes regime at 3.9×10^{-2} bar, 0.90 bar, and 10 bar. Thus, the transition points place limits on growth for these relatively small particles. The reason why the gap continues to deepen is that smaller particles settle more slowly than larger ones in the Stokes regime.

In Figure 13, we plot the distributions of mass density for all the size bins at the same seven different pressure

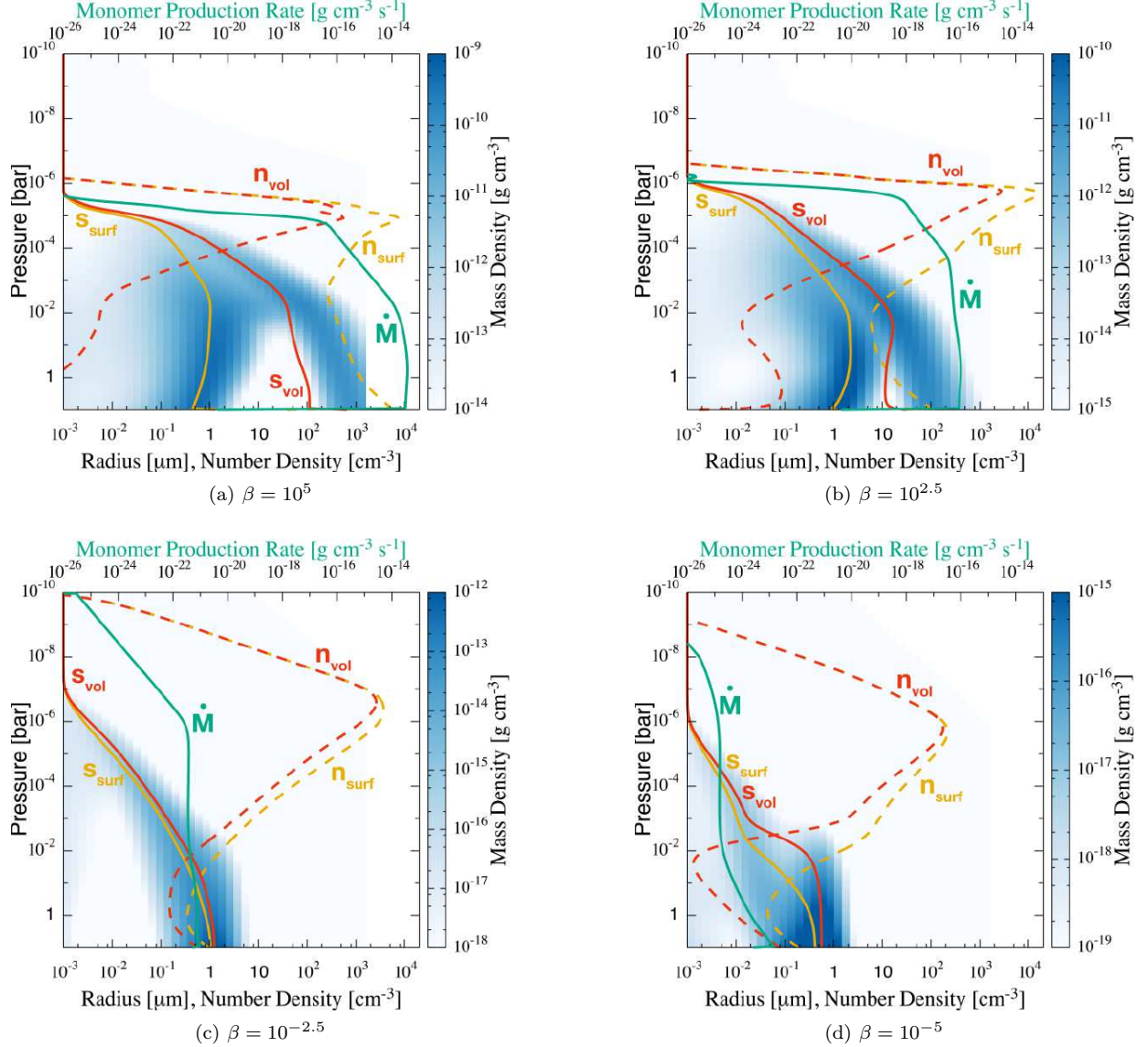


Figure 11. Same as Fig. 6 but for $\beta =$ (a) 10^5 , (b) $10^{2.5}$, (c) $10^{-2.5}$, and (d) 10^{-5} . See Eq. (35) for the definition of β .

levels as shown in Fig. 12 for the case of $\beta = 10^5$. In contrast to the case of $\beta = 1$ (Fig. 8), the distribution is clearly bimodal for the pressure levels, 3.9×10^{-2} bar, 0.15 bar, and 10 bar. The distributions of mass density are qualitatively similar to those of number density (Fig. 12). The obvious difference is that the two peaks of mass density are comparable in value.

Figure 14 shows the transmission spectrum models for the atmosphere with haze for the five cases where β is 10^5 (red line), $10^{2.5}$ (yellow line), 1 (green line, same as the green line in Fig. 9), $10^{-2.5}$ (blue line), and 10^{-5} (purple line). Transmission spectrum model for the atmosphere without haze in the case of $\beta = 1$ (black line) is also plotted, but can be hardly seen as it overlaps with that for the atmosphere with haze for $\beta = 10^{-5}$ (purple line). Similarly to Fig. 9, the horizontal dotted lines rep-

resent the transit depths corresponding to the pressure levels from 1×10^{-6} bar to 1 bar for the atmosphere in the case of $\beta = 1$. From this figure, we can see that the transmission spectrum varies with the value of β significantly. In the case of $\beta = 10^5$ (red line), the overall spectrum is rather flat. This is because the floating haze particles at high altitudes ($P \sim 10^{-5}$ bar) make the atmosphere so optically thick that their absorption obscures spectral absorption features due to the molecules in the lower ($P \gtrsim 10^{-5}$ bar) atmosphere. Also, it turns out that the bimodal size distribution seen in the range of $P \gtrsim 10^{-5}$ bar (see Fig. 11) hardly affects the resultant transmission spectrum. In the case of $\beta = 10^{2.5}$ (yellow line), some features of the haze can be seen, which include the spectral slope due to Rayleigh scattering in the optical and the absorption features at $3.0 \mu\text{m}$

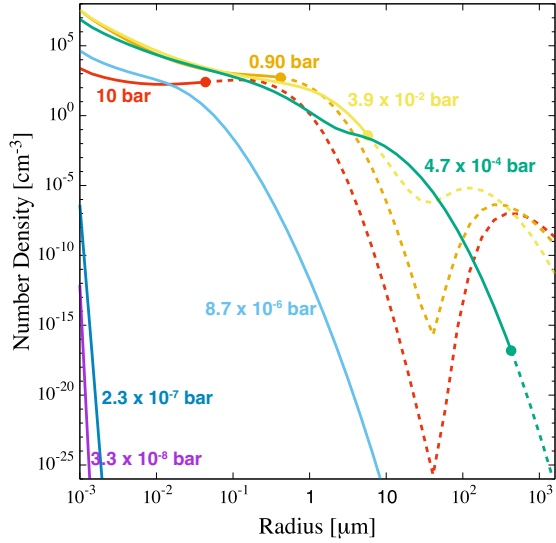


Figure 12. Distributions of number density for all the size bins at seven different pressure levels, 3.3×10^{-8} bar (purple line), 2.3×10^{-7} bar (blue line), 8.7×10^{-6} bar (light blue line), 4.7×10^{-4} bar (green line), 3.9×10^{-2} bar (yellow line), 0.90 bar (orange line), and 10 bar (red line) for the case of $\beta = 10^5$. The Stokes regime is indicated by dashed lines, while the slip flow regime is indicated by solid lines; The transition points are marked by filled circles.

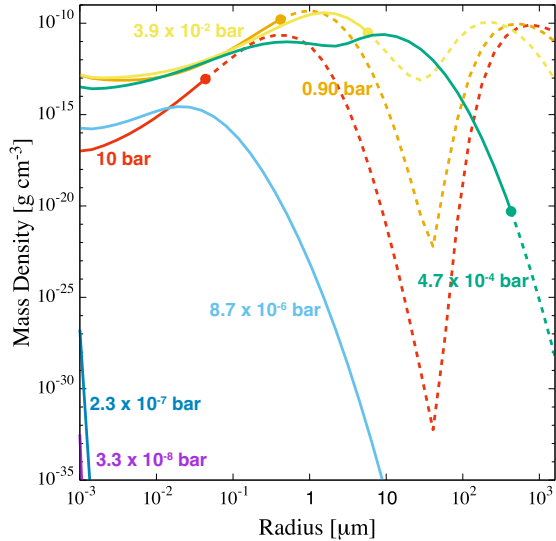


Figure 13. Same as Fig. 12 but the distribution of mass density.

and $4.6 \mu\text{m}$ coming from the vibrational transitions of the C-H and $\text{C}\equiv\text{N}$ bonds, respectively. As β decreases, the overall transit depth becomes lower. This is because the altitude at which the atmosphere becomes optically thick also decreases. In the case of $\beta = 10^{-5}$ (purple line), the spectrum is almost the same as that of the atmosphere without haze (black line). In conclusion, these results demonstrate that the difference in monomer production rate, which relates to the UV irradiation intensity from the host star, makes the diversity of trans-

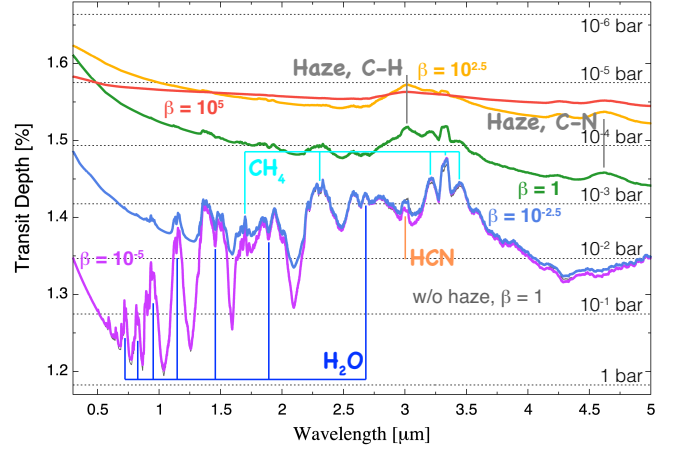


Figure 14. Transmission spectrum models for the atmosphere with haze for the five cases where β is 10^5 (red line), $10^{2.5}$ (yellow line), 1 (green line, same as the green line in Fig. 9), $10^{-2.5}$ (blue line), and 10^{-5} (purple line). Transmission spectrum model for the atmosphere without haze in the case of $\beta = 1$ (black line) is also plotted, but can be hardly seen as it overlaps with that for the atmosphere with haze in the case of $\beta = 10^{-5}$ (purple line). Same as Fig. 9, horizontal dotted lines represent the transit depths to the pressure levels from 1×10^{-6} bar to 1 bar for the atmosphere without haze in the case of $\beta = 1$. Note that the transmission spectrum models are smoothed for clarity.

mission spectrum: completely flat spectrum, spectrum with only extinction features of hazes (i.e., spectral slope due to Rayleigh scattering and absorption features of hazes), spectrum with slope due to Rayleigh scattering and some molecular absorption features, and spectrum with only molecular absorption features.

4. VALIDITY OF CHARACTERISTIC SIZE APPROXIMATION IN PARTICLE GROWTH CALCULATION

When comparing theoretical transmission spectra of hazy atmospheres with high-precision observational data, the distribution of haze particles has to be determined with multiple-size growth calculations (§ 2.2). To explore the possibility of reducing the computational cost and understand the effect of bimodality on transmission spectra, we examine the validity of characteristic size approximation quantitatively, applying the grain growth model of Ormel (2014). The characteristic size approximation assumes that there are particles of a single size and monomers in the atmosphere. This approximation is validated, at least, in the studies of the dynamics of dust grains in protoplanetary disks (Okuzumi et al. 2011) and proto-envelopes of gas giants (Ormel 2014).

We assume that the haze particle size distribution at any altitude z is characterized by a characteristic mass

m^* , defined as (Ormel 2014)

$$m^* \equiv \frac{\int \xi(m) m dm}{\int \xi(m) dm}, \quad (68)$$

where $\xi(m)$ is the distribution function of particles of mass m . The characteristic mass m^* changes by both coagulation of haze particles and production of monomers. The latter effect decreases the value of m^* toward the monomer mass. In this study, because focusing on the effect of size distribution, we neglect the gravitational collection and eddy diffusion, which are included in our particle growth module developed in § 2.2. Thus, we assume that coagulation occurs due to the Brownian collision only. The gravitational collection is important when both small and large particles are abundant. Thus, as shown in the previous section, this has a significant influence on the vertical profile of haze particles in the case of $\beta = 10^5$. However, as also shown above because the altitude where gravitational collection becomes important is optically thick enough for transmitted radiation, the exclusion of gravitational collection has a little effect on resultant transmission spectra. Also, as the particle transport mechanism, we take only gravitational sedimentation into account and ignore eddy diffusion. While the eddy diffusion affects the vertical profile of haze particles in the lower atmosphere in the case of $\beta = 10^{-5}$ to some extent, we ignore the effect because we want to focus on the effect of size distribution. The maximum differences in transit depth between spectrum models obtained from the multiple size calculations with and without two effects (gravitational collection and eddy diffusion) in the wavelength range of 0.3-5 μm are 38, 64, 43, 202, and 85ppm for $\beta = 10^5$, $10^{2.5}$, 1, $10^{-2.5}$, and 10^{-5} , respectively. The relatively large difference for $\beta = 10^{-2.5}$ case comes from the eddy diffusion effect.

Figure 15 shows the transmission spectrum models for the atmosphere with haze for the five cases where β is 10^5 (red line), $10^{2.5}$ (yellow line), 1 (green line), $10^{-2.5}$ (blue line), and 10^{-5} (purple line). Models obtained from the multiple size calculations (§ 2.2) are shown with thick lines, while those calculated with the characteristic size approximation are plotted with thin lines. The model for the haze-free atmosphere for $\beta = 1$ (black line) is also plotted. Same as Fig. 9, the horizontal dotted lines represent the transit depths corresponding to the pressure levels from 1×10^{-6} bar to 1 bar for the atmosphere without haze in the case of $\beta = 1$. Again, we ignore the gravitational collection and eddy diffusion also in the multiple-size particle growth calculations to compare the results from those with the characteristic size approximation.

In the case of $\beta = 10^5$ (red lines), although the size distribution is obviously bimodal in the lower atmosphere

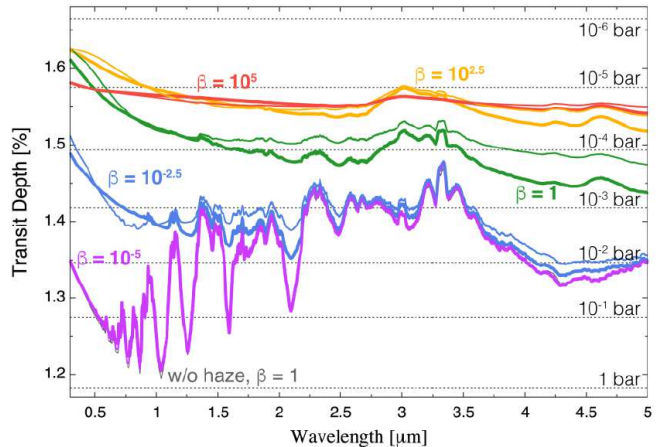


Figure 15. Transmission spectrum models for the atmosphere with haze for the five cases where the haze monomer production parameter β is 10^5 (red lines), $10^{2.5}$ (yellow lines), 1 (green lines), $10^{-2.5}$ (blue lines), and 10^{-5} (purple lines). Models obtained from the multiple size calculations (§ 2.2) are shown with thick lines, while those calculated with the characteristic size approximation are plotted with thin lines. Transmission spectrum model for the atmosphere without haze in the case of $\beta = 1$ (black line) is also plotted. Same as Fig. 9, the horizontal dotted lines represent the transit depths corresponding to the pressure levels from 1×10^{-6} bar to 1 bar for the atmosphere without haze in the case of $\beta = 1$. Note that the transmission spectra are smoothed for clarity.

(see Figs. 12 and 13), the difference between the two spectrum models are very small. This is because haze particles are so abundant that the atmosphere is optically thick at low pressures ($P \sim 10^{-5}$ bar) and therefore the difference in haze particle distribution in the lower atmosphere ($P \gtrsim 10^{-5}$ bar) hardly affects the resultant spectrum. In the case of the intermediate values of $\beta = 10^{2.5}$ (yellow lines), 1 (green lines), and $10^{-2.5}$ (blue lines), the differences between the two models are relatively large, because the size multiplicity is important. In the case of $\beta = 10^{-5}$ (purple lines), the difference in transit depth between the two models are relatively small because of their small abundance of haze in the atmosphere.

The maximum differences in transit depth between the two models in the wavelength range of 0.3-5 μm for $\beta = 10^5$, $10^{2.5}$, 1, $10^{-2.5}$, and 10^{-5} are 87, 205, 393, 393, and 101ppm, respectively. Precision of observed transit depths depends on properties of the planet, host star, observational instrument, and so on. If the precision of observed transit depths is larger than the difference in transit depth between the multiple-size and characteristic-size models, the characteristic size approximation is useful.

5. SUMMARY AND CONCLUSIONS

In this study, we have developed the transmission spectrum models of a close-in warm (~ 500 K) exo-

planet with a hazy hydrogen-dominated atmosphere by calculating directly the creation, growth, and settling of hydrocarbon haze particles to derive the distribution of haze particles. More specifically, we have done photochemical calculations to derive the vertical profiles of volume mixing ratios of the haze precursors, HCN and C₂H₂. Then, using the obtained vertical profiles of the precursors, we have calculated the growth and settling of haze particles in the atmosphere to derive the steady-state distribution of the size and number density of haze particles. We have also modeled transmission spectra of the atmospheres with obtained properties of hazes to explore whether the recently-observed diversity of transmission spectra can be explained by the variation in the production rate of haze monomers.

We have found that the haze particles tend to distribute in a wider region than previously assumed and consists of various sizes. We have also found that the difference in the production rate of haze monomers, which relates to the UV irradiation intensity from the host star, yields the diversity of transmission spectra observationally suggested: completely flat spectra, spectra with only extinction features of hazes (i.e., spectral slope due to Rayleigh scattering and absorption features of hazes), spectra with slope due to Rayleigh scattering and some molecular absorption features, and spectra with only molecular absorption features.

Also, by applying the grain growth model of [Ormel \(2014\)](#), we have examined the validity of characteristic size approximation in particle growth calculation. We have quantified the precisions of observed transit depths beyond which the characteristic approximation suffices to be used for comparison with observation.

In this paper, we have focused mainly on describing the methodology and demonstrating the sensitivity of transmission spectra to haze monomer production rate. In our forthcoming papers, we make detailed investigation of the dependence of transmission spectra on model parameters other than monomer production rate such as atmospheric metallicity, C/O ratio, eddy diffusion coefficient, atmospheric temperature profile, and monomer size. Also, we explore in detail the composition of the atmospheres of known warm exoplanets by comparing the observed spectra with our theoretical ones, taking into account other possibilities of cloud/haze constituents.

We would like to express special thanks to the following people. N. Narita and A. Fukui motivated us to work on this study and gave fruitful suggestions through observational collaboration. Advice and comments from Y. Sekine and S. Okuzumi were great help in modeling the properties of haze particles. Also, we had fruitful discussions with N. Iwagami, Y. Ito, and K. Kurosaki

regarding transmission spectrum modeling and with Y. Abe, H. Genda, Y. Miguel, and A. Youngblood regarding photochemical and thermochemical modeling. We are grateful to S.-M. Tsai for kindly providing us his calculation data for model comparison. We also thank the anonymous referee for his/her careful reading and constructive comments that helped us improve this paper greatly. Y. K. is supported by the Grant-in-Aid for JSPS Fellow (JSPS KAKENHI No. 15J08463) and Leading Graduate Course for Frontiers of Mathematical Sciences and Physics. M. I. is also supported by the Astrobiology Center Program of National Institutes of Natural Sciences (NINS) (No. AB291004) and JSPS Core-to-Core Program International Network of Planetary Sciences. This work has made use of the MUSCLES Treasury Survey High-Level Science Products.

APPENDIX

A. COMPARISON WITH Tsai et al. (2017)

To verify our photochemical model presented in section 2.1, we first examine our thermochemical reaction networks. In this section, we attempt to reproduce the results of Tsai et al. (2017) for two hot Jupiters, HD 189733b and HD 209458b. They considered thermochemistry and eddy-diffusion transport, but ignored photochemistry. They then simulated the atmospheric chemistry of these two planets to compare their models with those of Moses et al. (2011).

For comparison, we adopt the same assumptions and values of input parameters that Tsai et al. (2017) adopted: The fluxes of all the species are zero both at the lower and upper boundaries. The temperature profiles are the dayside-averaged ones taken from the supplementary material of Moses et al. (2011). The value of eddy diffusion coefficient K_{zz} is $1 \times 10^9 \text{ cm}^2 \text{ s}^{-1}$ and the solar elemental abundance ratios from Table 10 of Lodders et al. (2009). O abundance is multiplied by a factor of 0.793 to account for the effect of oxygen sequestration (see Moses et al. 2011). We prepare 90 layers with thickness of 50 km and 140 km for the simulations of HD 189733b and HD 209458b, respectively, and place the lower boundary pressure at 1000 bar. For the values of planet mass and 1000-bar radius, we use $1.15 M_J$ and $1.26 R_J$ for HD 189733b (Bouchy et al. 2005), and $0.685 M_J$ and $1.359 R_J$ for HD 209458b (Torres et al. 2008).

Figure A1 shows the calculated vertical distributions of gaseous species (solid lines) for the atmospheres of (a) HD 189733b and (b) HD 209458b, which are compared to the results of Tsai et al. (2017) (thin solid lines with crosses). HCN is not included in the model of Tsai et al. (2017), while the molecules indicated in italics are not included in our model. Vertical distributions of HCN from “no photon” models of Moses et al. (2011), in which they omit photochemistry, are also shown (thin solid lines with asterisks). We take these data by tracing their Figure 3 with the use of the software, PlotDigitizer X⁶. We also present the thermochemical equilibrium abundances with dashed lines for reference.

In the case of (a) HD 189733b first, the mixing ratios of ours and Tsai et al. (2017) differ by a factor of ~ 30 for CH_4 , ~ 4 for CO, and ~ 2 for H_2O , because quench occurs at higher pressure in our model. Because of such difference in f_{CH_4} , our abundances of CH_3 and CH_3OH are larger by 1-2 and 1-3 orders of magnitude, respectively. The abundances of species in thermochemical equilibrium such as CO_2 , H, and O match theirs well. As for haze precursors, since HCN is not considered in their models, we cannot do any comparison regarding HCN. However, the “no photon” models of Moses et al. (2011) (thin solid line with asterisks), in which they omit photochemistry, yield similar abundances to ours. The abundance of C_2H_2 differs little between Tsai et al. (2017)’s and ours. This slight difference in C_2H_2 abundance never affects our results regarding haze distributions and transmission spectra, since the profile of the production rate of monomers is determined mainly by that of HCN abundance (see § 3.1 and 3.4).

In the case of (b) HD 209458b, the abundances of the species, CO, H_2O , H, CH_4 , CO_2 , CH_3 , CH_3OH , and O, match theirs well. This is because of higher temperature of HD 209458b, for which the molecules tend to be closer to thermochemical equilibrium. As for haze precursors, we again compare the HCN abundance from our model with that from the “no photon” models of Moses et al. (2011). In our model, the abundance of HCN deviates from its thermochemical equilibrium values at higher pressure (~ 100 bar) compared to Moses et al. (2011) (~ 1 bar), and HCN results in being quenched at larger abundance in the pressure range of 1×10^{-3} bar to 100 bar. If we used the result of Moses et al. (2011) as the distribution of the precursor molecules, we would assume smaller monomer production at high altitudes and larger at low altitudes. This would hamper particle growth a little and result in less flat transmission spectra. The abundance of C_2H_2 is larger than that of Tsai et al. (2017) in the region where C_2H_2 is not in thermochemical equilibrium (i.e., $P \lesssim 10^{-1}$ bar). However, again, this difference never affects our results regarding haze distributions and transmission spectra, because the profile of the production rate of monomers is determined mainly by that of HCN abundance.

B. COMPARISON WITH Kopparapu et al. (2012)

In this section, we compare our photochemical model with the model of Kopparapu et al. (2012) for the hot Jupiter WASP-12b, in which photochemistry is considered in addition to thermochemistry and transport by eddy diffusion.

For comparison, we use the same profiles of temperature and eddy diffusion coefficient by tracing the Figure 1 of Kopparapu et al. (2012) with use of PlotDigitizer X. Following them, we neglect transport of the short-lived species $\text{O}(^1\text{D})$ and $^1\text{CH}_2$. Since the photodissociation reactions for CO, H_2 , N_2 , and CH_3OH are not taken into account in

⁶ <http://www.surf.nuqe.nagoya-u.ac.jp/nakahara/software/plotdigitizerx/index-e.html>

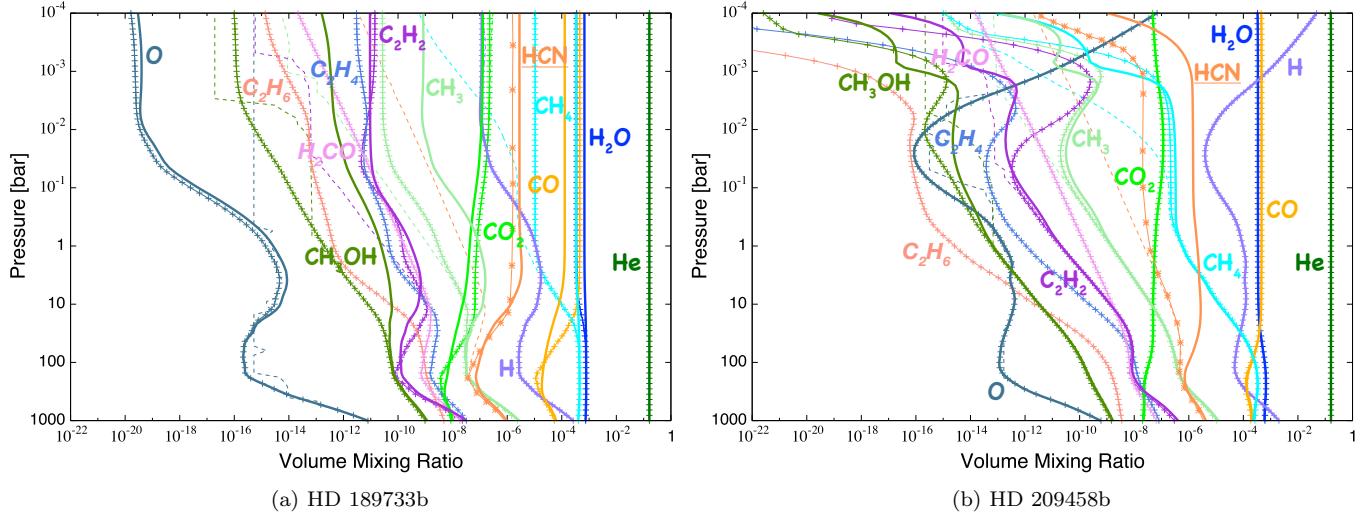
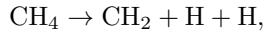


Figure A1. Vertical distributions of gaseous species (solid lines) for the atmospheres of (a) HD 189733b and (b) HD 209458b, compared to those from Tsai et al. (2017) (solid lines with crosses). HCN is not included in the model of Tsai et al. (2017) while the molecules indicated in italics are not included in our model. Vertical distributions of HCN from “no photon” models of Moses et al. (2011), in which they omit photochemistry, are also shown (thin solid lines with asterisks). We take these data by tracing their Figure 3 with the use of the software, PlotDigitizer X. We also present the thermochemical equilibrium abundances with dashed lines for reference. Note that the eddy diffusion transport is not included in the thermochemical equilibrium calculations.

their model, we exclude photochemical reactions, P7, P10, P11, and P12, from our photochemical reaction list used in this section. Also, while we consider the following photochemical reaction,



which they do not consider, they consider the following photochemical reaction,



which we do not consider. The other photochemical reactions are identical to theirs. Following them, we use the G0V star spectrum from Pickles (1998) and convert it to suit for WASP-12 by using the relation between the flux at 5556 Å and the visual magnitude, V , from Gray (1992). We use $V = 11.69$ (Hebb et al. 2009), 427 pc as the distance to the star (Chan et al. 2011), and 0.0229 AU as the semi-major axis (Hebb et al. 2009). We take the solar elemental abundance ratios from Table 1 of Asplund et al. (2005) following them. We prepare 100 layers with thickness of 128 km placing the lower boundary pressure at 1 bar. For the values of planet mass and 1-bar radius, we use $1.41 M_J$ and $1.79 R_J$, respectively (Hebb et al. 2009).

Figure B2 shows the calculated vertical distributions of gaseous species (solid lines), which are compared to the results of Kopparapu et al. (2012) (solid lines with symbols) that we also take by tracing their Figure 4 with the use of PlotDigitizer X. We also present the thermochemical equilibrium abundances with dashed lines for reference.

The abundances of the major ($f_i \gtrsim 10^{-10}$) species agree with Kopparapu et al. (2012)’s within one order of magnitude. The abundances at the lower boundary (1 bar) are slightly different from theirs, although we have used thermochemical equilibrium values for the lower boundary condition in the same way as they did and also used the same elemental abundance ratios. The differences in abundance profile may come from those in these lower boundary values.

C. THERMOCHEMICAL REACTIONS

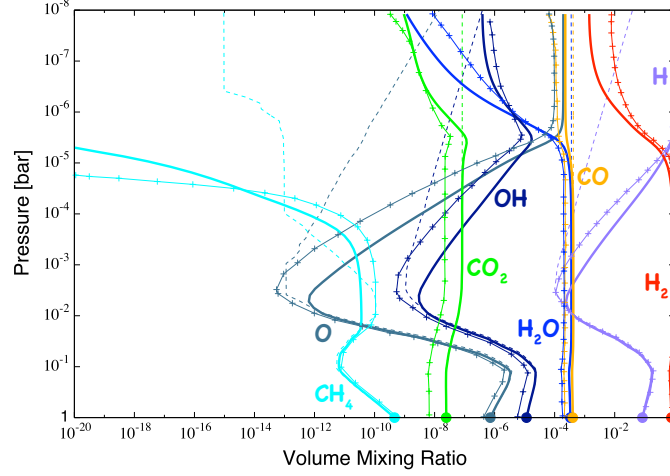


Figure B2. Vertical distributions of gaseous species (solid lines) compared to those from [Kopparapu et al. \(2012\)](#) (solid lines with symbols), which we take by tracing their Figure 4 with the use of PlotDigitizer X. Filled circles represent the thermochemical equilibrium values at the lower boundary. The thermochemical equilibrium abundances are shown with dashed lines for reference. Note that the eddy diffusion transport is not included in the thermochemical equilibrium calculations.

Table C1. Thermochemical Reactions

No.	No. Hu ^a	Reactants	Products	Rate Coefficients ^b	Ref.	Temp. ^c
R1	R1	C + CH ₂	→ CH + CH	$2.69 \times 10^{-12} e^{-23573.0/T}$	NIST	1000-4000
R2	R2	C + CN	→ C ₂ + N	$4.98 \times 10^{-10} e^{-18041.0/T}$	NIST	5000-8000
R3	R3	C + H ₂	→ CH + H	$6.64 \times 10^{-10} e^{-11700.0/T}$	NIST	1520-2540
R4	R5	C + N ₂	→ CN + N	$8.7 \times 10^{-11} e^{-22611.0/T}$	NIST	2000-5000
R5	R6	C + O ₂	→ CO + O	$5.1 \times 10^{-11} (T/298.0)^{-0.3}$	NIST	15-295
R6	R14	C ₂ H + CH ₃ OH	→ C ₂ H ₂ + CH ₃ O	2.0×10^{-12}	NIST	300-2500
R7	R17	C ₂ H ₂ + CN	→ HCN + C ₂ H	2.2×10^{-10}	NIST	294
R8	R31	CH + CH	→ C ₂ H ₂	2.0×10^{-10}	NIST	298
R9	R34	CH ₂ + C ₂ H	→ C ₂ H ₂ + CH	3.0×10^{-11}	NIST	300-2500
R10	R40	NH + OH	→ NH ₂ + O	$2.94 \times 10^{-12} (T/298.0)^{0.1} e^{5800.0/T}$	NIST	298-3000
R11	R42	CH ₂ + CH ₂	→ C ₂ H ₂ + H ₂	$2.62 \times 10^{-9} e^{-6010.0/T}$	NIST	1100-2700
R12	R43	CH ₂ + CH ₂	→ C ₂ H ₂ + H + H	$3.32 \times 10^{-10} e^{-5530.0/T}$	NIST	1100-2700
R13	R48	CH ₂ + CH ₄	→ CH ₃ + CH ₃	$7.12 \times 10^{-12} e^{-5050.0/T}$	NIST	296-707
R14	R49	CH ₂ + CH ₃ OH	→ CH ₃ + CH ₃ O	$1.12 \times 10^{-15} (T/298.0)^{3.1} e^{-3490.0/T}$	NIST	300-2500
R15	R50	CH ₂ + HCO	→ CO + CH ₃	3.0×10^{-11}	NIST	300-2500
R16	R57	CH ₃ + C ₂ H ₂	→ CH ₄ + C ₂ H	$3.0 \times 10^{-13} e^{-8700.0/T}$	NIST	300-2500
R17	R69	CH ₃ + CH ₃ OH	→ CH ₄ + CH ₃ O	$1.12 \times 10^{-15} (T/298.0)^{3.1} e^{-3490.0/T}$	NIST	300-2500
R18	R71	CH ₃ + HCO	→ CH ₄ + CO	2.0×10^{-10}	NIST	300-2500
R19	R91	CH ₄ + C ₂ H	→ C ₂ H ₂ + CH ₃	$3.0 \times 10^{-12} e^{-250.0/T}$	NIST	300-2500
R20	R96	CH ₄ + CH ₃ O	→ CH ₃ OH + CH ₃	$2.61 \times 10^{-13} e^{-4450.0/T}$	NIST	300-2500
R21	R99	CH ₄ + CN	→ HCN + CH ₃	$5.11 \times 10^{-13} (T/298.0)^{2.64} e^{150.3/T}$	NIST	290-1500
R22	R101	CH ₃ OH + CN	→ HCN + CH ₃ O	1.2×10^{-10}	NIST	294
R23	R108	HCO + C ₂ H	→ C ₂ H ₂ + CO	1.0×10^{-10}	NIST	300-2500
R24	R113	HCO + CH ₃ O	→ CH ₃ OH + CO	1.5×10^{-10}	NIST	300-2500
R25	R116	HCO + CN	→ HCN + CO	1.0×10^{-10}	NIST	500-2500

Table C1 continued

Table C1 (continued)

No.	No. Hu ^a	Reactants	Products	Rate Coefficients ^b	Ref.	Temp. ^c
R26	R120	CO + C ₂ H ₂	→ C ₂ H + HCO	$8.0 \times 10^{-10} e^{-53641.4/T}$	NIST	300-2500
R27	R122	CO + CH ₃	→ C ₂ H ₂ + OH	$6.3 \times 10^{-11} e^{-30428.9/T}$	NIST	1500-1900
R28	R127	H + C ₂ H	→ C ₂ H ₂	3.0×10^{-10}	NIST	300-2500
R29	R128	H + C ₂ H	→ H ₂ + C ₂	$6.0 \times 10^{-11} e^{-14192.0/T}$	NIST	300-2500
R30	R129	H + C ₂ H ₂	→ C ₂ H + H ₂	$1.0 \times 10^{-10} e^{-11200.0/T}$	NIST	300-2500
R31	R145	H + CH	→ C + H ₂	$1.31 \times 10^{-10} e^{-85.6/T}$	NIST	300-2000
R32	R146	H + CH ₂	→ CH + H ₂	$1.0 \times 10^{-11} e^{900.0/T}$	NIST	300-3000
R33	R149	H + CH ₃	→ CH ₂ + H ₂	$1.0 \times 10^{-10} e^{-7600.0/T}$	NIST	300-2500
R34	R152	H + CH ₃ O	→ CH ₃ OH	$2.89 \times 10^{-10} (T/298.0)^{0.04}$	NIST	300-2500
R35	R153	H + CH ₃ O	→ CH ₃ + OH	1.6×10^{-10}	NIST	300-2500
R36	R157	H + CH ₄	→ CH ₃ + H ₂	$5.83 \times 10^{-13} (T/298.0)^{3.0} e^{-4040.0/T}$	NIST	300-2500
R37	R158	H + CH ₃ OH	→ CH ₃ + H ₂ O	$3.32 \times 10^{-10} e^{-2670.0/T}$	NIST	1370-1840
R38	R159	H + CH ₃ OH	→ CH ₃ O + H ₂	$2.42 \times 10^{-12} (T/298.0)^{2.0} e^{-2270.0/T}$	NIST	300-2500
R39	R162	H + HCO	→ CO + H ₂	1.50×10^{-10}	NIST	300-2500
R40	R165	H + CO ₂	→ CO + OH	$2.51 \times 10^{-10} e^{-13350.0/T}$	NIST	300-2500
R41	R166	H + H ₂ O	→ H ₂ + OH	$6.82 \times 10^{-12} (T/298.0)^{1.6} e^{-9720.0/T}$	NIST	300-2500
R42	R184	H + NH	→ H ₂ + N	1.69×10^{-11}	NIST	1500-2500
R43	R185	H + NH ₂	→ H ₂ + NH	$1.05 \times 10^{-10} e^{-4450.1/T}$	NIST	1100-1800
R44	R186	H + NH ₃	→ H ₂ + NH ₂	$7.80 \times 10^{-13} (T/298.0)^{2.4} e^{-4990.1/T}$	NIST	490-1780
R45	R191	H + O ₂	→ O + OH	$6.73 \times 10^{-10} (T/298.0)^{-0.59} e^{-8152.0/T}$	NIST	800-3500
R46	R193	H ₂ + C	→ CH + H	$6.64 \times 10^{-10} e^{-11700.0/T}$	NIST	1520-2540
R47	R194	H ₂ + C ₂	→ C ₂ H + H	$1.1 \times 10^{-10} e^{-4000.0/T}$	NIST	2580-4650
R48	R195	H ₂ + C ₂ H	→ C ₂ H ₂ + H	$8.95 \times 10^{-13} (T/298.0)^{2.57} e^{-130.0/T}$	NIST	200-2000
R49	R202	H ₂ + CH	→ CH ₂ + H	$3.75 \times 10^{-10} e^{-1660.0/T}$	NIST	327-397
R50	R203	H ₂ + CH ₃	→ CH ₄ + H	$6.86 \times 10^{-14} (T/298.0)^{2.74} e^{-4740.0/T}$	NIST	300-2500
R51	R204	H ₂ + CH ₃ O	→ CH ₃ OH + H	$9.96 \times 10^{-14} (T/298.0)^2 e^{-6720.0/T}$	NIST	300-2500
R52	R207	H ₂ + CN	→ HCN + H	$5.65 \times 10^{-13} (T/298.0)^{2.45} e^{-1131.0/T}$	NIST	300-2500
R53	R211	H ₂ + NH	→ NH ₂ + H	$3.5 \times 10^{-11} e^{-7758.0/T}$	NIST	833-1432
R54	R212	H ₂ + NH ₂	→ NH ₃ + H	$6.75 \times 10^{-14} (T/298.0)^{2.6} e^{-3006.8/T}$	NIST	400-2200
R55	R214	H ₂ O + C	→ CH + OH	$1.3 \times 10^{-12} e^{-19845.0/T}$	NIST	1000-4000
R56	R215	H ₂ O + C ₂ H	→ C ₂ H ₂ + OH	$7.74 \times 10^{-14} (T/298.0)^{3.05} e^{-376.0/T}$	NIST	300-2000
R57	R218	H ₂ O + CH	→ CH ₃ O	$9.48 \times 10^{-12} e^{380.0/T}$	NIST	298-669
R58	R219	H ₂ O + CN	→ HCN + OH	$1.3 \times 10^{-11} e^{-3760.0/T}$	NIST	500-2500
R59	R276	N + C ₂	→ CN + C	2.8×10^{-11}	NIST	298
R60	R280	N + CH	→ C + NH	$3.0 \times 10^{-11} (T/298.0)^{0.65} e^{-1203.0/T}$	NIST	990-1010
R61	R281	N + CH	→ CN + H	$1.66 \times 10^{-10} (T/298.0)^{-0.09}$	NIST	216-584
R62	R282	N + CH ₃	→ H ₂ + HCN	$4.3 \times 10^{-10} e^{-420.0/T}$	NIST	200-423
R63	R284	N + CN	→ C + N ₂	3.0×10^{-10}	NIST	300-2500
R64	R287	N + H ₂ O	→ OH + NH	$6.03 \times 10^{-11} (T/298.0)^{1.2} e^{-19243.6/T}$	NIST	800-3000
R65	R289	N + NH	→ N ₂ + H	$1.95 \times 10^{-11} (T/298.0)^{0.51} e^{-9.6/T}$	NIST	300-2500
R66	R290	N + NH ₂	→ NH + NH	$3.0 \times 10^{-13} e^{-7600.0/T}$	NIST	1000-4000
R67	R300	NH + NH ₃	→ NH ₂ + NH ₂	$5.25 \times 10^{-10} e^{-13470.0/T}$	NIST	1300-1700
R68	R305	NH + O	→ OH + N	1.16×10^{-11}	NIST	250-3000

Table C1 continued

Table C1 (continued)

No.	No. Hu ^a	Reactants	Products	Rate Coefficients ^b	Ref.	Temp. ^c
R69	R309	NH + OH	→ H ₂ O + N	$3.1 \times 10^{-12} (T/298.0)^{1.2}$	NIST	298-3000
R70	R310	NH ₂ + C	→ CH + NH	$9.61 \times 10^{-13} e^{-10500.0/T}$	NIST	1000-4000
R71	R311	NH ₂ + C ₂ H ₂	→ C ₂ H + NH ₃	$8.2 \times 10^{-13} e^{-2780.0/T}$	NIST	340-510
R72	R316	NH ₂ + CH ₃	→ CH ₄ + NH	$8.4 \times 10^{-10} e^{-4834.9/T}$	NIST	300-2000
R73	R317	NH ₂ + CH ₄	→ CH ₃ + NH ₃	$8.77 \times 10^{-15} (T/298.0)^3 e^{-2130.0/T}$	NIST	300-2000
R74	R319	NH ₂ + H ₂ O	→ OH + NH ₃	$2.1 \times 10^{-13} (T/298.0)^{1.9} e^{-5725.0/T}$	NIST	300-3000
R75	R323	NH ₂ + O	→ OH + NH	1.16×10^{-11}	NIST	298-3000
R76	R326	NH ₂ + OH	→ H ₂ O + NH	$7.69 \times 10^{-13} (T/298.0)^{1.5} e^{-230.0/T}$	NIST	250-3000
R77	R327	NH ₃ + CH	→ HCN + H ₂ + H	$7.24 \times 10^{-11} e^{317.0/T}$	NIST	300-1300
R78	R328	NH ₃ + CH ₃	→ CH ₄ + NH ₂	$9.55 \times 10^{-14} e^{-4895.0/T}$	NIST	350-600
R79	R329	NH ₃ + CN	→ HCN + NH ₂	1.66×10^{-11}	NIST	300-700
R80	R388	O + C ₂	→ CO + C	6.0×10^{-10}	NIST	8000
R81	R389	O + C ₂ H	→ CO + CH	1.7×10^{-11}	NIST	300-2500
R82	R391	O + C ₂ H ₂	→ CO + CH ₂	$3.49 \times 10^{-12} (T/298.0)^{1.5} e^{-850.0/T}$	NIST	300-2500
R83	R407	O + CH	→ OH + C	$2.52 \times 10^{-11} e^{-2380.0/T}$	NIST	10-6000
R84	R408	O + CH	→ CO + H	6.6×10^{-11}	NIST	300-2000
R85	R409	O + CH ₂	→ CH + OH	7.2×10^{-12}	NIST	300-2500
R86	R410	O + CH ₂	→ HCO + H	5.0×10^{-11}	NIST	1200-1800
R87	R411	O + CH ₂	→ CO + H + H	1.2×10^{-10}	NIST	300-2500
R88	R412	O + CH ₂	→ CO + H ₂	7.3×10^{-11}	NIST	300-2500
R89	R414	O + CH ₃	→ CH ₃ O	$7.51 \times 10^{-14} (T/298.0)^{-2.12} e^{-314.0/T}$	NIST	300-2500
R90	R416	O + CH ₃	→ CO + H ₂ + H	5.72×10^{-11}	NIST	290-900
R91	R420	O + CH ₃ O	→ CH ₃ + O ₂	2.5×10^{-11}	NIST	298
R92	R423	O + CH ₄	→ CH ₃ + OH	$2.26 \times 10^{-12} (T/298.0)^{2.2} e^{-3820.0/T}$	NIST	420-1520
R93	R424	O + CH ₃ OH	→ CH ₃ O + OH	$1.66 \times 10^{-11} e^{-2360.0/T}$	NIST	300-1000
R94	R426	O + HCO	→ CO + OH	5.0×10^{-11}	NIST	300-2500
R95	R427	O + HCO	→ CO ₂ + H	5.0×10^{-11}	NIST	300-2500
R96	R430	O + CN	→ CO + N	$3.4 \times 10^{-11} e^{-210.0/T}$	NIST	500-2500
R97	R433	O + H ₂	→ H + OH	$3.44 \times 10^{-13} (T/298.0)^{2.67} e^{-3160.0/T}$	NIST	300-2500
R98	R436	O + HCN	→ CO + NH	$3.0 \times 10^{-12} e^{-4000.0/T}$	JPL	470-900
R99	R445	O + OH	→ O ₂ + H	$2.2 \times 10^{-11} e^{120.0/T}$	JPL	200-300
R100	R449	O(¹ D) + CH ₄	→ CH ₃ O + H	3.5×10^{-11}	JPL	200-300
R101	R450	O(¹ D) + CH ₄	→ CH ₃ + OH	1.31×10^{-10}	JPL	200-300
R102	R453	O(¹ D) + CH ₃ OH	→ CH ₃ O + OH	4.2×10^{-10}	NIST	300
R103	R454	O(¹ D) + CO ₂	→ CO ₂ + O	$7.5 \times 10^{-11} e^{115.0/T}$	JPL	200-300
R104	R455	O(¹ D) + H ₂	→ H + OH	1.2×10^{-10}	JPL	200-300
R105	R456	O(¹ D) + H ₂ O	→ OH + OH	$1.63 \times 10^{-10} e^{60.0/T}$	JPL	200-300
R106	R458	O(¹ D) + N ₂	→ O + N ₂	$2.15 \times 10^{-11} e^{110.0/T}$	JPL	200-300
R107	R461	O(¹ D) + NH ₃	→ OH + NH ₂	2.5×10^{-10}	JPL	200-300
R108	R464	O(¹ D) + O ₂	→ O + O ₂	$3.3 \times 10^{-11} e^{55.0/T}$	JPL	200-300
R109	R476	OH + C ₂	→ CO + CH	8.3×10^{-12}	NIST	2200
R110	R477	OH + C ₂ H	→ CO + CH ₂	3.0×10^{-11}	NIST	300-2500
R111	R478	OH + C ₂ H	→ C ₂ H ₂ + O	3.0×10^{-11}	NIST	300-2500

Table C1 continued

Table C1 (continued)

No.	No. Hu ^a	Reactants	Products	Rate Coefficients ^b	Ref.	Temp. ^c
R112	R480	OH + C ₂ H ₂	→ C ₂ H + H ₂ O	$1.03 \times 10^{-13} (T/298.0)^{2.68} e^{-6060.0/T}$	NIST	300-2500
R113	R482	OH + C ₂ H ₂	→ CO + CH ₃	$6.34 \times 10^{-18} (T/298.0)^{4.0} e^{1010.0/T}$	NIST	500-2500
R114	R495	OH + CH ₃	→ CH ₃ O + H	$6.45 \times 10^{-13} (T/298.0)^1 e^{-6012.0/T}$	NIST	300-3000
R115	R496	OH + CH ₃	→ CH ₂ + H ₂ O	$1.2 \times 10^{-10} e^{-1400.0/T}$	NIST	300-1000
R116	R501	OH + CH ₄	→ CH ₃ + H ₂ O	$2.45 \times 10^{-12} e^{-1775.0/T}$	JPL	200-300
R117	R502	OH + CH ₃ OH	→ CH ₃ O + H ₂ O	$2.9 \times 10^{-12} e^{-345.0/T}$	JPL	200-300
R118	R504	OH + HCO	→ CO + H ₂ O	1.69×10^{-10}	NIST	300-2500
R119	R507	OH + CN	→ O + HCN	$1.0 \times 10^{-11} e^{-1000.0/T}$	NIST	500-2500
R120	R511	OH + CO	→ CO ₂ + H	$5.4 \times 10^{-14} (T/298.0)^{1.5} e^{250.0/T}$	NIST	300-2000
R121	R512	OH + H ₂	→ H ₂ O + H	$2.8 \times 10^{-12} e^{-1800.0/T}$	JPL	200-300
R122	R515	OH + HCN	→ CO + NH ₂	$1.1 \times 10^{-13} e^{-5890.0/T}$	NIST	500-2500
R123	R516	OH + HCN	→ CN + H ₂ O	$1.84 \times 10^{-13} (T/298.0)^{1.5} e^{-3890.0/T}$	NIST	298-2840
R124	R523	OH + NH ₃	→ H ₂ O + NH ₂	$1.7 \times 10^{-12} e^{-710.0/T}$	JPL	200-300
R125	R526	OH + OH	→ H ₂ O + O	1.8×10^{-12}	JPL	200-300
R126	R596	¹ CH ₂ + H ₂	→ CH ₂ + H ₂	1.26×10^{-11}	YD99 ^d	
R127	R597	¹ CH ₂ + H ₂	→ CH ₃ + H	9.24×10^{-11}	YD99 ^d	
R128	R598	¹ CH ₂ + CH ₄	→ CH ₂ + CH ₄	1.2×10^{-11}	YD99 ^d	
R129	R599	¹ CH ₂ + CH ₄	→ CH ₃ + CH ₃	5.9×10^{-11}	YD99 ^d	
R130	R608	C ₂ + CH ₄	→ C ₂ H + CH ₃	$5.05 \times 10^{-11} e^{-297.0/T}$	YD99 ^d	
R131	R644	NH ₂ + OH	→ NH ₃ + O	$3.32 \times 10^{-13} (T/298.0)^{0.4} e^{-250.2/T}$	NIST	250-3000
R132	M1	C + C	→ C ₂	$5.46 \times 10^{-31} (T/298.0)^{-1.6} \times M$	NIST	5000-6000
R133	M2	C + H ₂	→ CH ₂	$6.89 \times 10^{-32} \times M$	NIST	300
R134	M11	H + CN	→ HCN	$9.35 \times 10^{-30} (T/298.0)^{-2.0} e^{-521.0/T} \times M$	NIST	500-2500
R135	M12	H + CO	→ HCO	$5.29 \times 10^{-34} e^{-370.0/T} \times M$	NIST	300-2500
R136	M13	H + H	→ H ₂	$6.04 \times 10^{-33} (T/298.0)^{-1.0} \times M$	NIST	300-2500
R137	M14	H + NH ₂	→ NH ₃	$3.0 \times 10^{-30} \times M$	NIST	298
R138	M16	H + O	→ OH	$4.36 \times 10^{-32} (T/298.0)^{-1.0} \times M$	NIST	300-2500
R139	M18	H + OH	→ H ₂ O	$6.87 \times 10^{-31} (T/298.0)^{-2.0} \times M$	NIST	300-3000
R140	M22	N + C	→ CN	$9.4 \times 10^{-33} \times M$	NIST	298
R141	M23	N + H	→ NH	$5.0 \times 10^{-32} \times M$	NIST	298
R142	M24	N + H ₂	→ NH ₂	$1.0 \times 10^{-36} \times M$	NIST	298
R143	M25	N + N	→ N ₂	$1.38 \times 10^{-33} e^{502.7/T} \times M$	JPL	90-6400
R144	M30	O + C	→ CO	$2.0 \times 10^{-34} \times M$	NIST	8000
R145	M31	O + CO	→ CO ₂	$1.7 \times 10^{-33} e^{-1509.0/T} \times M$	NIST	300-2500
R146	M34	O + O	→ O ₂	$5.21 \times 10^{-35} e^{900.0/T} \times M$	NIST	200-4000
R147	M55	H + CH ₂	→ CH ₃	$k_0^e = 5.8 \times 10^{-30} e^{355.0/T}$ $k_\infty^e = 2.37 \times 10^{-12} e^{523.0/T}$	YD99 ^d	
R148	M56	H + CH ₃	→ CH ₄	$6.2 \times 10^{-29} (T/298.0)^{-1.8} \times M$	NIST	300-1000
R149	M72	CH + H ₂	→ CH ₃	$k_0^e = 5.8 \times 10^{-30} e^{355.0/T}$ $k_\infty^e = 2.37 \times 10^{-12} e^{523.0/T}$	YD99 ^d	
R150	T19	CH ₃ OH	→ CH ₃ O + H	$2.16 \times 10^{-8} e^{-33556.0/T} \times M$	NIST	1400-2500
R151	T20	CH ₃ OH	→ CH ₃ + OH	$1.1 \times 10^{-7} e^{-33075.0/T} \times M$	NIST	1000-2000
R152	T22	CH ₃ OH	→ CH ₂ + H ₂ O	$9.51 \times 10^{15} (T/298.0)^{-1.02} e^{-46185.0/T}$	NIST	1000-3000

Table C1 (*continued*)

No.	No. Hu ^a	Reactants	Products	Rate Coefficients ^b	Ref.	Temp. ^c
R153	T46	HCO	→ CO + H	$6.0 \times 10^{-11} e^{-7721.0/T} \times M$	NIST	298-1229
R154	T57	HCN	→ H + CN	$1.93 \times 10^{-4} (T/298.0)^{-2.44} e^{-62782.1/T} \times M$	NIST	1800-5000

^aReaction number of [Hu et al. \(2012\)](#)

^bUnit of $\text{cm}^3 \text{s}^{-1}$ for 2-body reactions and $\text{cm}^6 \text{s}^{-2}$ for 3-body reactions

^cUnit of K

^d[Yung & Demore \(1999\)](#)

^eRate coefficient k : $k = \left(\frac{k_0 M}{1 + \frac{k_0 M}{k_\infty}} \right) 0.6 \left[1 + \left(\log_{10} \frac{k_0 M}{k_\infty} \right)^2 \right]^{-1}$

NOTE—Thermochemical Reactions used in our photochemical model. M refers to the number density of background atmosphere (unit of cm^{-3}). We assume M equals to the total number density.

D. PHOTOCHEMICAL REACTIONS

Table D2. Photochemical Reactions

No.	No. Hu ^a	Reactants	Products	Quantum Yields
P1	1	O ₂	→ O + O	$\lambda < 139 \text{ nm}$: 0.5 $139 \text{ nm} \leq \lambda < 175 \text{ nm}$: 0 $\lambda \geq 175 \text{ nm}$: 1.0
P2	2	O ₂	→ O + O(¹ D)	$\lambda < 139 \text{ nm}$: 0.5 $139 \text{ nm} \leq \lambda < 175 \text{ nm}$: 1.0 $\lambda \geq 175 \text{ nm}$: 0
P3	6	H ₂ O	→ H + OH	1.0
P4	32	CH ₄	→ CH ₃ + H	0.41 (Smith & Raulin 1999)
P5	33	CH ₄	→ CH ₂ ¹ + H ₂	0.53 (Smith & Raulin 1999)
P6	34	CH ₄	→ CH + H ₂ + H	0.06 (Smith & Raulin 1999)
P7	35	CO	→ C + O	$\lambda < 111 \text{ nm}$: 1.0 $\lambda \geq 111 \text{ nm}$: 0
P8	36	CO ₂	→ CO + O	$\lambda < 167 \text{ nm}$: 0 $167 \text{ nm} \leq \lambda < 205 \text{ nm}$: 1.0 $\lambda \geq 205 \text{ nm}$: 0
P9	37	CO ₂	→ CO + O(¹ D)	$\lambda < 167 \text{ nm}$: 1.0 $\lambda \geq 167 \text{ nm}$: 0
P10	38	H ₂	→ H + H	$\lambda < 80 \text{ nm}$: 0.1 (Mentall & Gentieu 1970) $80 \text{ nm} \leq \lambda < 85 \text{ nm}$: 1.0 $\lambda \geq 85 \text{ nm}$: 0
P11	39	N ₂	→ N + N	1.0
P12	40	CH ₃ OH	→ CH ₃ O + H	1.0
P13	41	HCN	→ H + CN	1.0
P14	42	NH ₃	→ NH ₂ + H	$\lambda < 106 \text{ nm}$: 0.3 (Lilly et al. 1973)

Table D2 continued

Table D2 (*continued*)

No.	No. Hu ^a	Reactants	Products	Quantum Yields
				106 nm \leq λ < 165 nm: Linear interpolation $\lambda \geq$ 165 nm: 1.0
P15	43	NH ₃	\rightarrow NH + H ₂	λ < 106 nm: 0.7 106 nm \leq λ < 165 nm: Linear interpolation $\lambda \geq$ 165 nm: 1.0
P16	55	C ₂ H ₂	\rightarrow C ₂ H + H	λ < 217 nm: 1.0 (Läuter et al. 2002) $\lambda \geq$ 217 nm: 0

^aReaction number of Hu et al. (2012)

^bWe use the polynomial expansion written in page 4D-3 of Sander et al. (2011).

NOTE—Photochemical Reactions used in our photochemical model and values of quantum yields.

E. UV CROSS SECTIONS

Table E3. UV Cross Sections

Species	Wavelength	Cross Sections	T ^a
O ₂	4.13 nm \leq λ \leq 103.00 nm	Brion et al. (1979)	N
	108.75 nm \leq λ \leq 129.60 nm	Ogawa & Ogawa (1975)	N
	129.62 nm \leq λ \leq 172.53 nm	Yoshino et al. (2005)	N
	176.8 nm \leq λ \leq 202.6 nm	Kockarts (1976)	N
	205 nm \leq λ \leq 245 nm	Sander et al. (2011)	N
H ₂ O	6.20 nm \leq λ \leq 118.08 nm	Chan et al. (1993b)	N
	121.00 nm \leq λ \leq 198.00 nm	Sander et al. (2011)	N
	198.00 nm \leq λ \leq 240 nm	Extrapolation	
CH ₄	52.054 nm \leq λ \leq 124.629 nm	Kameta et al. (2002)	N
	125 nm \leq λ \leq 141 nm	Chen & Wu (2004)	N
	142 nm \leq λ \leq 152 nm	Lee et al. (2001)	N
CO	6.199 nm \leq λ \leq 177 nm	Chan et al. (1993a)	N
CO ₂	35.0000 nm \leq λ \leq 197.6950 nm	Huestis & Berkowitz (2010)	N
	197.70 nm \leq λ \leq 270.15 nm	Ityaksov et al. (2008)	N
H ₂	18 nm \leq λ \leq 70 nm	Lee et al. (1976)	N
	77.00 nm \leq λ \leq 86.88 nm	Cook & Metzger (1964)	N
	88.6 nm \leq λ \leq 124 nm	Backx et al. (1976)	N
N ₂	6.199 nm \leq λ \leq 113 nm	Chan et al. (1993c)	N
CH ₃ OH	15.5 nm \leq λ \leq 103 nm	Burton et al. (1992)	N
	106.50 nm \leq λ \leq 165.00 nm	Nee et al. (1985)	N
	165.5 nm \leq λ \leq 219.5 nm	Cheng et al. (2002)	N
HCN	133.42 nm \leq λ \leq 144.75 nm	Macpherson & Simons (1978)	N
NH ₃	8.0 nm \leq λ \leq 105.0 nm	Samson et al. (1987)	N
	106.00 nm \leq λ \leq 139.98 nm	Wu et al. (2007)	N

Table E3 continued

Table E3 (*continued*)

Species	Wavelength	Cross Sections	T ^a
	140.00 nm $\leq \lambda \leq$ 230.00 nm	Cheng et al. (2006)	N
C ₂ H ₂	6.20 nm $\leq \lambda \leq$ 131 nm	Cooper et al. (1995)	N
	136.90378 nm $\leq \lambda \leq$ 185.62863 nm	Smith et al. (1991)	Y
	185.63 nm $\leq \lambda \leq$ 236.290 nm	Bénilan et al. (2000)	Y

^aTemperature dependence: Y and N indicate whether temperature dependence is taken into account or not.

^bWe use the expression written in page 4D-2 of [Sander et al. \(2011\)](#).

REFERENCES

- Allen, M., Yung, Y. L., & Waters, J. W. 1981, *J. Geophys. Res.*, 86, 3617
- Anglada-Escudé, G., Rojas-Ayala, B., Boss, A. P., Weinberger, A. J., & Lloyd, J. P. 2013, *A&A*, 551, A48
- Armitage, P. J. . 2010, *Astrophysics of Planet Formation* (New York: Cambridge University Press)
- Asplund, M., Grevesse, N., & Sauval, A. J. 2005, in *Astronomical Society of the Pacific Conference Series*, Vol. 336, *Cosmic Abundances as Records of Stellar Evolution and Nucleosynthesis*, ed. T. G. Barnes, III & F. N. Bash, 25
- Awiphan, S., Kerins, E., Pichadee, S., et al. 2016, *MNRAS*, 463, 2574
- Backx, C., Wight, G. R., & Van der Wiel, M. J. 1976, *Journal of Physics B Atomic Molecular Physics*, 9, 315
- Bénilan, Y., Smith, N., Jolly, A., & Raulin, F. 2000, *Planet. Space Sci.*, 48, 463
- Biddle, L. I., Pearson, K. A., Crossfield, I. J. M., et al. 2014, *MNRAS*, 443, 1810
- Bohren, C. F., & Huffman, D. R. 2004, *Absorption and Scattering of Light by Small Particles* (Weinheim: Wiley-VCH)
- Bouchy, F., Udry, S., Mayor, M., et al. 2005, *A&A*, 444, L15
- Brion, C., Tan, K., van der Wiel, M., & van der Leeuw, P. 1979, *Journal of Electron Spectroscopy and Related Phenomena*, 17, 101
- Brown, T. M. 2001, *ApJ*, 553, 1006
- Burton, G. R., Chan, W. F., Cooper, G., & Biron, C. E. 1992, *Chemical Physics*, 167, 349
- Cantrell, J. R., Henry, T. J., & White, R. J. 2013, *AJ*, 146, 99
- Chan, T., Ingemyr, M., Winn, J. N., et al. 2011, *AJ*, 141, 179
- Chan, W. F., Cooper, G., & Brion, C. E. 1993a, *Chemical Physics*, 170, 123
- . 1993b, *Chemical Physics*, 178, 387
- Chan, W. F., Cooper, G., Sodhi, R. N. S., & Brion, C. E. 1993c, *Chemical Physics*, 170, 81
- Charbonneau, D., Berta, Z. K., Irwin, J., et al. 2009, *Nature*, 462, 891
- Chen, F. Z., & Wu, C. Y. R. 2004, *JQSRT*, 85, 195
- Cheng, B.-M., Bahou, M., Lee, Y.-P., & Lee, L. C. 2002, *Journal of Geophysical Research (Space Physics)*, 107, 1161
- Cheng, B.-M., Lu, H.-C., Chen, H.-K., et al. 2006, *ApJ*, 647, 1535
- Cook, G. R., & Metzger, P. H. 1964, *Journal of the Optical Society of America (1917-1983)*, 54, 968
- Cooper, G., Olney, T. N., & Brion, C. E. 1995, *Chemical Physics*, 194, 175
- Crossfield, I. J. M., Barman, T., Hansen, B. M. S., & Howard, A. W. 2013, *A&A*, 559, A33
- Davies, C. N. 1945, *Proceedings of the Physical Society*, 57, 259
- de Mooij, E. J. W., Brogi, M., de Kok, R. J., et al. 2012, *A&A*, 538, A46
- Dragomir, D., Benneke, B., Pearson, K. A., et al. 2015, *ApJ*, 814, 102
- Ehrenreich, D., Bonfils, X., Lovis, C., et al. 2014, *A&A*, 570, A89
- Fischer, J., Gamache, R. R., Goldman, A., Rothman, L. S., & Perrin, A. 2003, *JQSRT*, 82, 401
- Fortney, J. J., Marley, M. S., & Barnes, J. W. 2007, *ApJ*, 659, 1661
- France, K., Parke Loyd, R. O., Youngblood, A., et al. 2016, *ApJ*, 820, 89
- Fukui, A., Narita, N., Kurosaki, K., et al. 2013, *ApJ*, 770, 95
- Fukui, A., Kawashima, Y., Ikoma, M., et al. 2014, *ApJ*, 790, 108
- Fukui, A., Narita, N., Kawashima, Y., et al. 2016, *ApJ*, 819, 27
- Grassi, T., Bovino, S., Schleicher, D. R. G., et al. 2014, *MNRAS*, 439, 2386
- Gray, D. F. 1992, *The observation and analysis of stellar photospheres*.
- Guillot, T. 2010, *A&A*, 520, A27
- Haynes, W. M. 2012, *CRC HANDBOOK OF CHEMISTRY and PHYSICS*, 92nd edn. (CRC Press)
- Hebb, L., Collier-Cameron, A., Loeillet, B., et al. 2009, *ApJ*, 693, 1920
- Helling, C., & Woitke, P. 2006, *A&A*, 455, 325
- Heng, K. 2016, *ApJL*, 826, L16
- Heng, K., & Kitzmann, D. 2017, *MNRAS*, 470, 2972
- Hindmarsh, A. C. 1982, *IMACS Trans. Sci. Comput.*, 1, 55
- Howe, A. R., & Burrows, A. S. 2012, *ApJ*, 756, 176
- Hu, R., Seager, S., & Bains, W. 2012, *ApJ*, 761, 166
- Huestis, D. L., & Berkowitz, J. 2010, in *Bulletin of the American Astronomical Society*, Vol. 42, *AAS/Division for Planetary Sciences Meeting Abstracts #42*, 972
- Husser, T.-O., Wende-von Berg, S., Dreizler, S., et al. 2013, *A&A*, 553, A6
- Ityaksov, D., Linnartz, H., & Ubachs, W. 2008, *Chemical Physics Letters*, 462, 31
- Jacobson, M. Z. M. Z. 2005, *Fundamentals of atmospheric modeling / Mark Z. Jacobson*, 2nd edn., Vol. : pbk; : hard (New York: Cambridge University Press), xiv, 813 p.

- Kameta, K., Kouchi, N., Ukai, M., & Hatano, Y. 2002, *Journal of Electron Spectroscopy and Related Phenomena*, 123, 225, determination of cross-sections and momentum profiles of atoms, molecules and condensed matter
- Khare, B. N., Sagan, C., Arakawa, E. T., et al. 1984, *Icarus*, 60, 127
- Knutson, H. A., Benneke, B., Deming, D., & Homeier, D. 2014, *Nature*, 505, 66
- Kockarts, G. 1976, *Planet. Space Sci.*, 24, 589
- Kopparapu, R. k., Kasting, J. F., & Zahnle, K. J. 2012, *ApJ*, 745, 77
- Kreidberg, L., Bean, J. L., Désert, J.-M., et al. 2014, *Nature*, 505, 69
- Kuntz, M. 1997, *JQSRT*, 57, 819
- Lanotte, A. A., Gillon, M., Demory, B.-O., et al. 2014, *A&A*, 572, A73
- Läuter, A., Lee, K. S., Jung, K. H., et al. 2002, *Chemical Physics Letters*, 358, 314
- Lavvas, P., Yelle, R. V., & Griffith, C. A. 2010, *Icarus*, 210, 832
- Lecavelier Des Etangs, A., Pont, F., Vidal-Madjar, A., & Sing, D. 2008, *A&A*, 481, L83
- Lee, A. Y. T., Yung, Y. L., Cheng, B.-M., et al. 2001, *ApJL*, 551, L93
- Lee, L. C., Carlson, R. W., & Judge, D. L. 1976, *JQSRT*, 16, 873
- Lilly, R., Rebbert, R., & Ausloos, P. 1973, *Journal of Photochemistry*, 2, 49
- Line, M. R., Vasisht, G., Chen, P., Angerhausen, D., & Yung, Y. L. 2011, *ApJ*, 738, 32
- Linsky, J. L., Fontenla, J., & France, K. 2014, *ApJ*, 780, 61
- Liou, K. N. 2002, *An Introduction to Atmospheric Radiation*, 2nd edn. (Amsterdam: Academic Press)
- Lodders, K. 2003, *ApJ*, 591, 1220
- Lodders, K., Palme, H., & Gail, H.-P. 2009, *Landolt Börnstein*, arXiv:0901.1149
- Loyd, R. O. P., France, K., Youngblood, A., et al. 2016, *ApJ*, 824, 102
- Macpherson, M. T., & Simons, J. P. 1978, *J. Chem. Soc., Faraday Trans. 2*, 74, 1965
- McKay, C. P., Coustenis, A., Samuelson, R. E., et al. 2001, *Planet. Space Sci.*, 49, 79
- Mentall, J. E., & Gentieu, E. P. 1970, *JChPh*, 52, 5641
- Mie, G. 1908, *Annalen der Physik*, 330, 377
- Miguel, Y., & Kaltenegger, L. 2014, *ApJ*, 780, 166
- Miller-Ricci, E., & Fortney, J. J. 2010, *ApJL*, 716, L74
- Miller-Ricci Kempton, E., Zahnle, K., & Fortney, J. J. 2012, *ApJ*, 745, 3
- Morley, C. V., Fortney, J. J., Kempton, E. M.-R., et al. 2013, *ApJ*, 775, 33
- Moses, J. I., Visscher, C., Fortney, J. J., et al. 2011, *ApJ*, 737, 15
- Moses, J. I., Line, M. R., Visscher, C., et al. 2013, *ApJ*, 777, 34
- Narita, N., Fukui, A., Ikoma, M., et al. 2013, *ApJ*, 773, 144
- Nascimbeni, V., Piotto, G., Pagano, I., et al. 2013, *A&A*, 559, A32
- Nascimbeni, V., Mallonn, M., Scandariato, G., et al. 2015, *A&A*, 579, A113
- Nee, J. B., Suto, M., & Lee, L. C. 1985, *Chemical Physics*, 98, 147
- Ogawa, S., & Ogawa, M. 1975, *Canadian Journal of Physics*, 53, 1845
- Okuzumi, S., Tanaka, H., Takeuchi, T., & Sakagami, M.-a. 2011, *ApJ*, 731, 95
- Ormel, C. W. 2014, *ApJL*, 789, L18
- Petty, G. W. 2006, *A First Course in Atmospheric Radiation*, 2nd edn. (Madison, Wis.: Sundog Pub.)
- Pickles, A. J. 1998, *PASP*, 110, 863
- Rothman, L. S., Rinsland, C. P., Goldman, A., et al. 1998, *JQSRT*, 60, 665
- Rothman, L. S., Gordon, I. E., Babikov, Y., et al. 2013, *JQSRT*, 130, 4
- Ruyten, W. 2004, *JQSRT*, 86, 231
- Samson, J. A. R., Haddad, G. N., & Kilcoyne, L. D. 1987, *JChPh*, 87, 6416
- Sander, S. P., Friedl, R. R., Abbatt, J. P. D., et al. 2011, *Chemical Kinetics and Photochemical Data for Use in Atmospheric Studies Evaluation Number 17 (JPL Publication)*
- Seager, S., & Deming, D. 2010, *ARA&A*, 48, 631
- Sharp, C. M., & Burrows, A. 2007, *ApJS*, 168, 140
- Sing, D. K., Wakeford, H. R., Showman, A. P., et al. 2015, *MNRAS*, 446, 2428
- Sing, D. K., Fortney, J. J., Nikolov, N., et al. 2016, *Nature*, 529, 59
- Smith, N. S., & Raulin, F. 1999, *J. Geophys. Res.*, 104, 1873
- Smith, P. L., Yoshino, K., Parkinson, W. H., Ito, K., & Stark, G. 1991, *J. Geophys. Res.*, 96, 17
- Smith, R. K., Brickhouse, N. S., Liedahl, D. A., & Raymond, J. C. 2001, *ApJL*, 556, L91
- Smith, W. R., & Missen, R. W. 1982, *Chemical Reaction Equilibrium Analysis: Theory and Algorithms (New York: A Wiley-Interscience Publication)*
- Stevenson, K. B. 2016, *ApJL*, 817, L16
- Tomasko, M. G., Doose, L. R., Dafoe, L. E., & See, C. 2009, *Icarus*, 204, 271
- Toon, O. B., McKay, C. P., Griffith, C. A., & Turco, R. P. 1992, *Icarus*, 95, 24
- Toon, O. B., Turco, R. P., & Pollack, J. B. 1980, *Icarus*, 43, 260
- Torres, G., Winn, J. N., & Holman, M. J. 2008, *ApJ*, 677, 1324
- Trainer, M. G., Pavlov, A. A., Dewitt, H. L., et al. 2006, *Proceedings of the National Academy of Science*, 103, 18035
- Tsai, S.-M., Lyons, J. R., Grosheintz, L., et al. 2017, *ApJS*, 228, 20
- Venot, O., Agúndez, M., Selsis, F., Tessenyi, M., & Iro, N. 2014, *A&A*, 562, A51
- Venot, O., Hébrard, E., Agúndez, M., Decin, L., & Bounaceur, R. 2015, *A&A*, 577, A33
- Venot, O., Hébrard, E., Agúndez, M., et al. 2012, *A&A*, 546, A43
- Visscher, C., & Moses, J. I. 2011, *ApJ*, 738, 72
- Woitke, P., & Helling, C. 2003, *A&A*, 399, 297
- . 2004, *A&A*, 414, 335
- Wu, Y.-J., Lu, H.-C., Chen, H.-K., et al. 2007, *JChPh*, 127, 154311
- Yoshino, K., Parkinson, W. H., Ito, K., & Matsui, T. 2005, *Journal of Molecular Spectroscopy*, 229, 238
- Youngblood, A., France, K., Parke Loyd, R. O., et al. 2016, *ApJ*, 824, 101
- Yung, Y. L., Allen, M., & Pinto, J. P. 1984, *ApJS*, 55, 465
- Yung, Y. L., & Demore, W. B., eds. 1999, *Photochemistry of planetary atmospheres*
- Zahnle, K., Marley, M. S., Morley, C. V., & Moses, J. I. 2016, *ApJ*, 824, 137
- Zahnle, K. J., & Marley, M. S. 2014, *ApJ*, 797, 41